Claremont Colleges
Scholarship @ Claremont

HMC Senior Theses   HMC Student Scholarship

2001

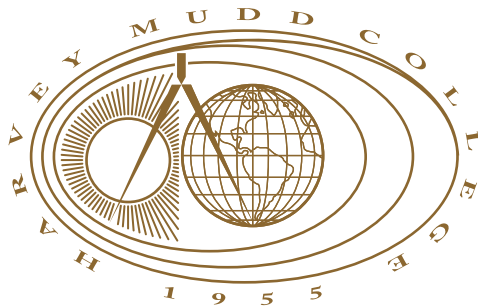# Computational Simulation of Fluid Dynamics in Thin Films

Anand Patil
Harvey Mudd College

Recommended Citation

Overturning Droplets in Thin Fluid Films

by

Anand Patil

Andrew Bernoff, Advisor

Advisor: _____

Second Reader: _____

(Tom Donnelly)

May 2001

Department of Mathematics

HARVEY MUDD
C O L L E G E

Abstract

Overturning Droplets in Thin Fluid Films

by Anand Patil

May 2001

We investigate the formation of droplets in a thin liquid film on a solid substrate due to the combined action of surface tension and van der Waals forces. Current models for droplet formation assume that droplets have a shallow profile. By removing that assumption and numerically solving for stable droplet profiles, we have modelled droplets that separate from the substrate on which they sit.

Table of Contents

List of Figures

Acknowledgments

I would like to thank Professor Andrew Bernoff for advising me on the writing of my thesis, Professor Keller and Professor Kuenning for helping me code, Professor Eckert for talking to me about the Van der Waals forces, and Professor Donnelly for agreeing to be my second reader.

Dedication

For Sonya

Chapter 1

Introduction

Figure 1 shows the evolution of oil on a thread as detergent is added to the water in which it is immersed. The detergent's effect is to reduce the surface interaction energy between the oil and the surrounding water, making it energetically favorable for the oil to expose relatively more of its surface to the surrounding water and relatively less of its surface to the thread. As the surface interaction energy is decreased, the oil film breaks up into droplets which become steeper. Eventually, the interfaces of the droplets overturn, and when surface energy is sufficiently weak the droplets separate from the thread. In this thesis, I will investigate similar behavior in much thinner films of 100 to $1000\mathring{A}$, whose dynamics are driven mainly by surface interactions and the Van der Waals forces. In this thickness regime, surface tension tends to flatten films' surfaces, while the Van der Waals forces tend to destabilize flat films and cause the formation of droplets.

The dynamics of very thin fluid films are generally modeled using lubrication theory, which assumes that the films have a low aspect ratio and that their interfaces never become very steep. Lubrication theory clearly cannot be used to model overturning droplets, as their surfaces are vertical in places. In addition, Bertozzi *et al.* [7] have demonstrated that as precursor film depth approaches zero the height of droplets predicted by lubrication theory becomes infinite- a highly unphysical result. The purpose of this project is to solve for equilibrium droplet profiles and their stability without using the lubrication approximation, and thereby model
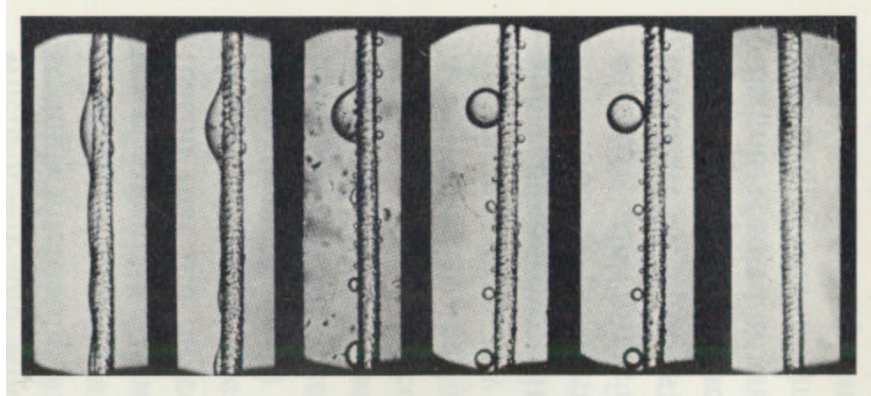
Figure 1.1: Oil droplets being removed from a thread by detergent

overturning droplets.

1.1 Physical background

Molecules whose time-averaged dipole moment is zero can temporarily develop dipole moments due to quantum mechanical fluctuations in their electron distribution [18]. If a molecule develops a dipole moment in this fashion, its electric field tends to induce parallel dipole moments in its neighbors, and strictly attractive intermolecular forces result. These attractive dipole-induced dipole forces are known as the Van der Waals forces, and their magnitude can be shown to vary with the distance r between the two molecules as $1/r^7$ (See appendix A) The Van der Waals forces are generally active over distances of 100-$1000\mathring{A}$, and they can be the dominant bulk forces driving the dynamics of fluid films whose depth is in this range.

We will model a fluid l sitting on a substrate s immersed in a surrounding fluid v that is uniform in one direction and constrained in a box in the other (fig. 1.2.) The energy of such a fluid is

$$E = \int\int_{interface} k \, dA + \int\int\int_{bulk} V_{ls} + V_{ll} + V_{fv} + V_{sv} + V_{vv} + V_{ss} + V_{lv} dV \quad (1.1)$$

Here dA is an infinitesimal surface element, dV is an infinitesimal volume element, and k is a constant with dimensions of energy per unit area. The first integral accounts for surface interaction energy between the fluid and the surrounding fluid, which is proportional to the area of the interface. The surface interactions between the fluid and substrate and the surrounding fluid and substrate are constant, since the area of contact between the fluid and the substrate is constant. The first term,V_{ls}, under the second integral is the Van der Waals potential energy of a differential fluid element due to its substrate, the second term V_{ll} is its energy due to the rest of the fluid, and so on. The bulk fluid-fluid, fluid-surrounding fluid, and surrounding fluid-surrounding fluid energies are assumed to be very small compared to the other energy terms due to the small surface area/volume ratio of very thin fluid films; these will be neglected. The substrate-surrounding fluid and substrate-substrate energies are nearly constant if the fluid is constrained in a box and if the fluid does not deform the substrate, so they may also be dropped from the equation. If the width of the box is L, the total remaining energy of a cross section of the fluid is, after nondimensionalization,

$$E = \int_0^L \sqrt{1 + h_x^2} - \frac{a}{h^2} + \frac{b}{h^3} dx \qquad (1.2)$$

The first term is the interface length between the fluid and the surrounding fluid, and the second two terms account for the Van der Waals fluid-substrate interaction. The form of this interaction is derived in Appendix A.
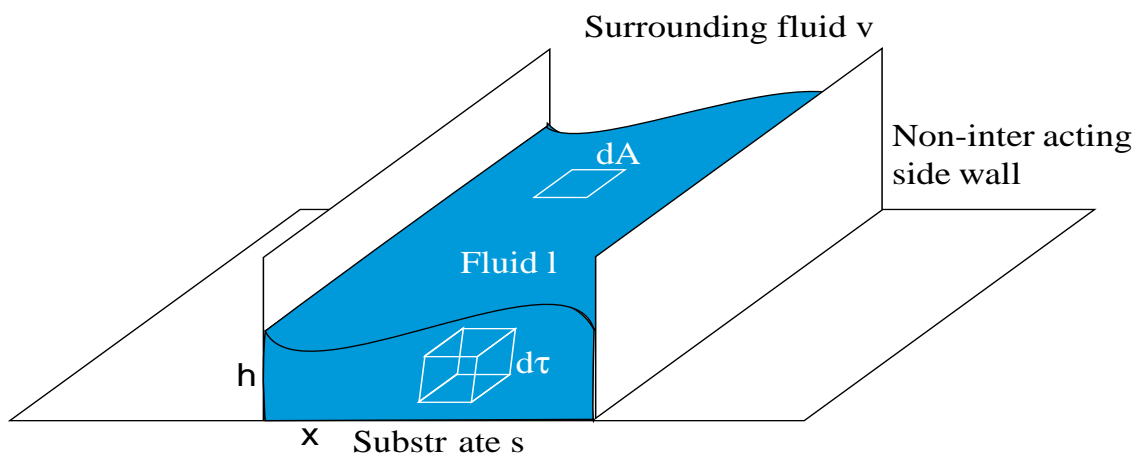
Figure 1.2: A liquid droplet L on a substrate S in a vapor V.

Chapter 2

The lubrication model

2.1   The analytical model

We begin our adventure by finding equilibrium fluid interfaces under the lubrication model. This model assumes that the height h and slope h_x of the fluid interface above the substrate at point x are very small, so that the differential interface length $(\sqrt{1 + h_x^2})dx$ may be approximated to first order as $(1 + \frac{1}{2}h_x^2)dx$. The energy under this model is

$$E = \int_0^L \frac{1}{2}h_x^2 - \frac{a}{h^2} + \frac{b}{h^3}dx \qquad (2.1)$$

where the constant 1 in the approximate interface length may be ignored as it shifts the energy by a constant.

An interface h is an equilibrium interface if the addition of a volume-preserving perturbation $\epsilon\hat{h}$ to it, where ϵ is a vanishingly small constant, leaves the energy

$$E(h + \epsilon\hat{h}) \approx E(h) + \epsilon\frac{\delta E}{\delta h} + \frac{1}{2}\epsilon^2\frac{\delta^2 E}{\delta h^2} \qquad (2.2)$$

unchanged to first order in ϵ. The term of order ϵ in equation (2.2) is

$$\begin{aligned}
\frac{\delta E}{\delta h} &= \int_0^L h_x\hat{h}_x + \hat{h}\left(\frac{2a}{h^3} - \frac{3b}{h^4}\right)dx \\
&= h_x\hat{h}\big|_{x=0}^L + \int_0^L \hat{h}\left(-h_{xx} + \frac{2a}{h^3} - \frac{3b}{h^4}\right)dx
\end{aligned} \qquad (2.3)$$

In order for the interface h to be stationary with respect to all volume- preserving
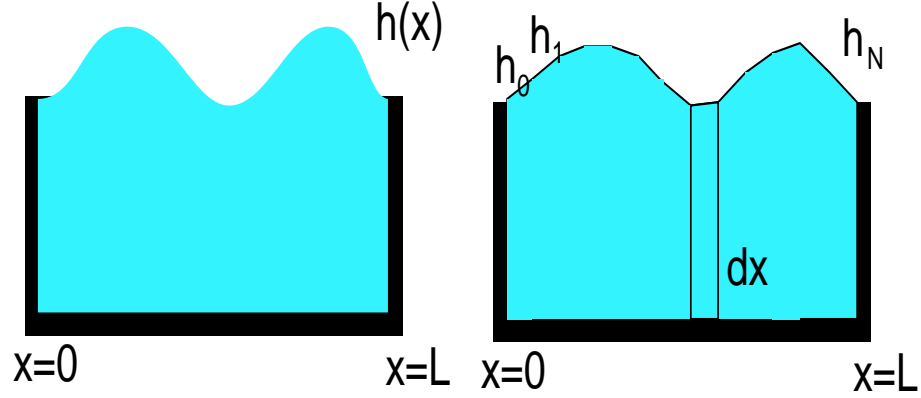
Figure 2.1: Approximating the continuous fluid shape as a series of trapezoidal columns

perturbations $\hat{h}$, h_x must be equal to zero at the box boundaries $x = 0, L$ and the pressure

$$P = -h_{xx} + \frac{2a}{h^3} - \frac{3b}{h^4} \tag{2.4}$$

must be constant for all values of x.

Bertozzi et al. [7] found equilibrium interfaces by solving the differential equation (2.4); we find them using a Newton-Raphson method [8], which I explain in the next section. The advantage of this method is that it makes it easier to determine the interfaces' stability. If the term of order ϵ^2 in (2.2) is positive definite for all $\hat{h}$ that preserve volume and become flat at the box boundary, then h is a stable equilibrium, and if it is not then h is unstable.

2.2 Numerical results

In order to find equilibrium interfaces numerically, we approximate the fluid as a series of discrete fluid columns (fig. 2.1).

If we divide the fluid into N columns of width $\Delta x = \frac{L}{N}$, then the height function $h(x)$ becomes a vector $\vec{h} = <h_1, h_2, ...h_N>$ and the energy becomes

$$E = \Delta x \sum_{i=1}^{N-1} \left[(\frac{1}{2} \frac{h_{i+1} - h_i}{\Delta x})^2 + \frac{V(h_{i+1}) + V(h_i)}{2} + \lambda \frac{h_{i+1} - h_i}{2} \right] - \lambda vol \qquad (2.5)$$

where V is the Van der Waals potential energy and λ is a Lagrange multiplier which constrains the fluid's volume. The discretized version of the energy expansion (2.2) is

$$E(\vec{p} + \epsilon \hat{p}) \approx E(\vec{p}) + \epsilon \hat{p} \cdot \vec{F}(\vec{p}) + \frac{\epsilon^2}{2} \hat{p}^T J(\vec{p}) \hat{p} \qquad (2.6)$$

where

$$\vec{p} = \begin{bmatrix} h_1 \\ h_2 \\ \vdots \\ h_N \\ \lambda \end{bmatrix}, \vec{F}(\vec{p}) = \begin{bmatrix} \frac{\partial E}{\partial h_1} \\ \frac{\partial E}{\partial h_2} \\ \vdots \\ \frac{\partial E}{\partial h_N} \\ \frac{\partial E}{\partial \lambda} \end{bmatrix}, J(\vec{p}) = \begin{bmatrix} \frac{\partial^2 E}{\partial h_1^2} & \frac{\partial^2 E}{\partial h_1 \partial h_2} & \cdots & \frac{\partial^2 E}{\partial h_1 \partial h_N} & \frac{\partial^2 E}{\partial h_1 \partial \lambda} \\ \frac{\partial^2 E}{\partial h_2 \partial h_1} & \frac{\partial^2 E}{\partial h_2^2} & \cdots & \frac{\partial^2 E}{\partial h_2 \partial h_N} & \frac{\partial^2 E}{\partial h_2 \partial \lambda} \\ \vdots & \vdots & \ddots & \vdots & \vdots \\ \frac{\partial^2 E}{\partial h_N \partial h_1} & \frac{\partial^2 E}{\partial h_N \partial h_2} & \cdots & \frac{\partial^2 E}{\partial h_N^2} & \frac{\partial^2 E}{\partial h_N \partial \lambda} \\ \frac{\partial^2 E}{\partial \lambda \partial h_1} & \frac{\partial^2 E}{\partial \lambda \partial h_2} & \cdots & \frac{\partial^2 E}{\partial \lambda \partial h_N} & \frac{\partial^2 E}{\partial \lambda^2} \end{bmatrix}$$

$$(2.7)$$

The parameters $\vec{p}$ constitute a stationary solution if $\vec{F}$, which contains the partial derivative of the energy with respect to each element of $\vec{p}$ and also with respect to λ, is zero. The stability of $\vec{p}$ is determined by the Jacobian matrix J; this is discussed further in section (3.3.) We use the Newton-Raphson method [8], an iterative root-finding method, to bring $\vec{F}$ to zero:

$$\vec{p}^{k+1} = \vec{p}^k - J(\vec{p}^k)^{-1} \vec{F}(\vec{p}^k) \qquad (2.8)$$

We find three classes of equilibrium solutions. One is the trivial flat solution (fig. 2.2), $\vec{h} = \bar{h}$, the second is an unstable solution (fig. 2.3), and the third is a stable solution, which for large volumes approximates a parabolic droplet (fig. 2.4)

sitting on an ultra-thin film whose thickness minimizes the Van der Waals potential energy.

$$\frac{dV(h)}{dh} = 0 \Rightarrow h = h_{min} \equiv \frac{3b}{2a} \tag{2.9}$$

The bifurcation of the droplet solution is easy to explain physically: as the film gets deeper, it eventually becomes energetically favorable for most of the film to be pulled down to the equilibrium depth h_{min}. This ultra-thin film is known as the precursor film. The remaining fluid takes on a parabolic shape because a parabola minimizes the approximate surface energy. If the surface energy is small relative to the Van der Waals potential, therefore, a long precursor film and tall droplet will be energetically favorable, and if the surface energy is large the parabolic droplet will be shallow and long, leaving a relatively small portion of the substrate covered by precursor film. Bertozzi *et al.* [7] found, in addition, that as the depth of the precursor film approaches zero the steepness and height of the parabolic droplet approach infinity (fig. 2.5.)

2.3   Linear stability of the flat solution

The location of bifurcations from the flat solution can be computed analytically. Perturbing the flat interface $h(x) = \bar{h}$ to form $\bar{h} + \epsilon\hat{h}$, where $\int_0^L \hat{h}dx = 0$ and $\hat{h}_x(0) = \hat{h}_x(L) = 0$ and expanding E about $E(\bar{h})$,

$$E = \int_0^L \frac{\epsilon^2}{2}\hat{h}_x^2 + V(\bar{h}) + \epsilon\hat{h}\frac{dV(\bar{h})}{d\bar{h}} + \frac{(\epsilon\hat{h})^2}{2}\frac{d^2V(\bar{h})}{d\bar{h}^2} + O(\epsilon^3)dx \tag{2.10}$$

The integral of the term of order ϵ is equal to zero, indicating that $h = \bar{h}$ is always a stationary solution. The terms of order ϵ^2 contain the stability information: when $h = \bar{h}$ is stable energy increases with the amplitude ϵ of the perturbation and these terms are positive, indicating that $h = \bar{h}$ is a local minimum of energy. When $\bar{h}$ is
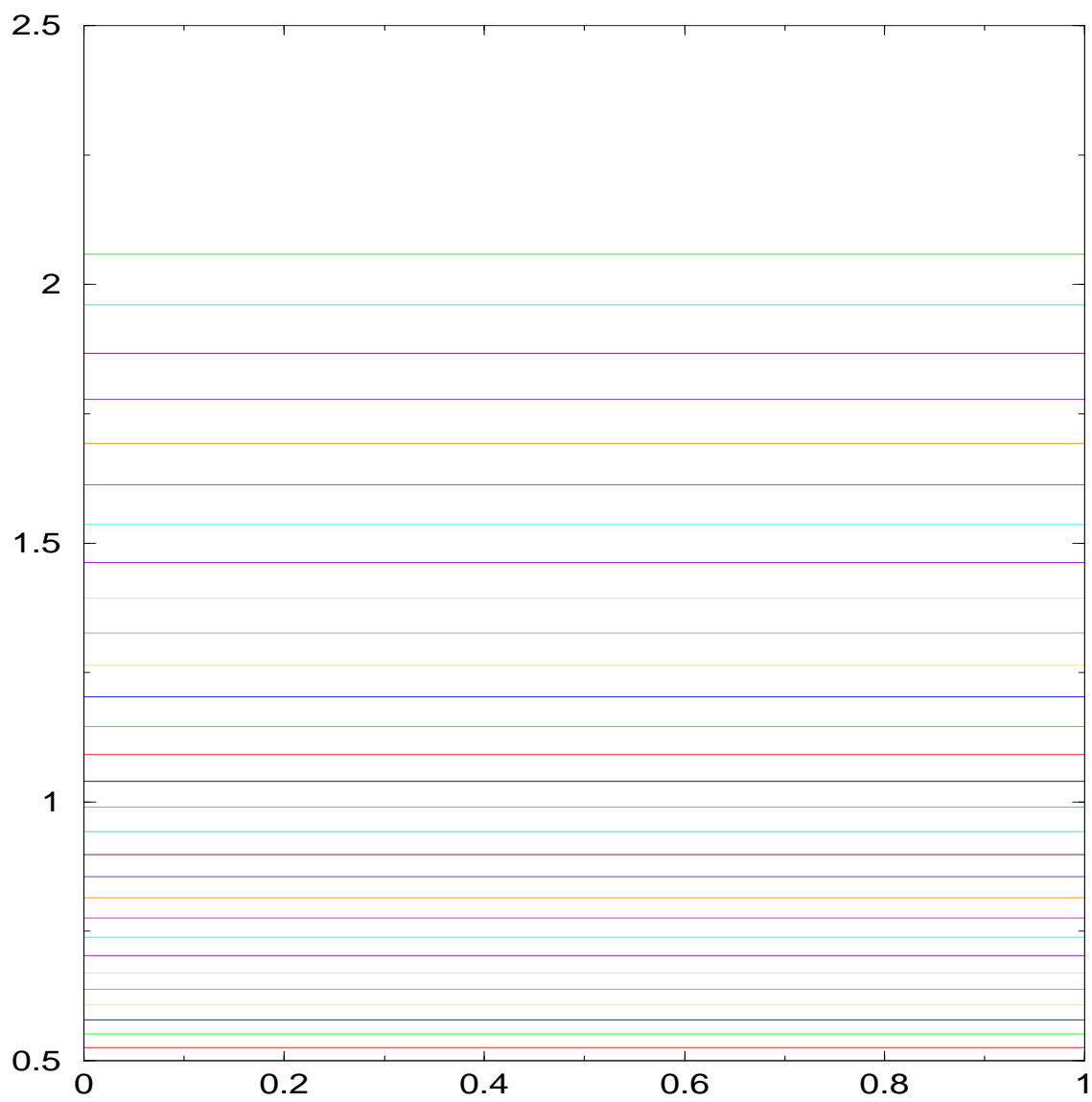
Figure 2.2: Flat solution for a=5, b=.3, L=1. Solutions are plotted for various volumes.

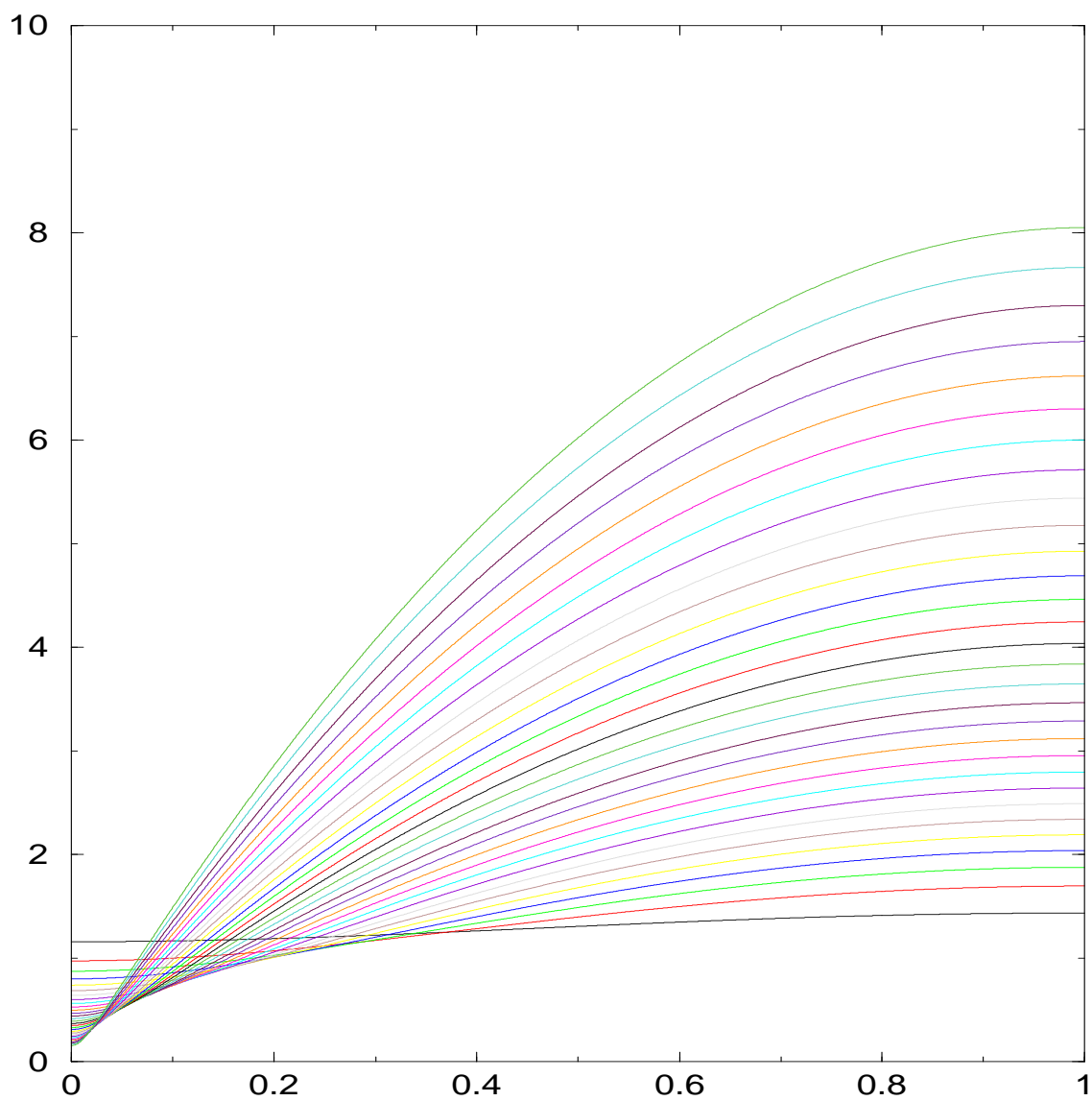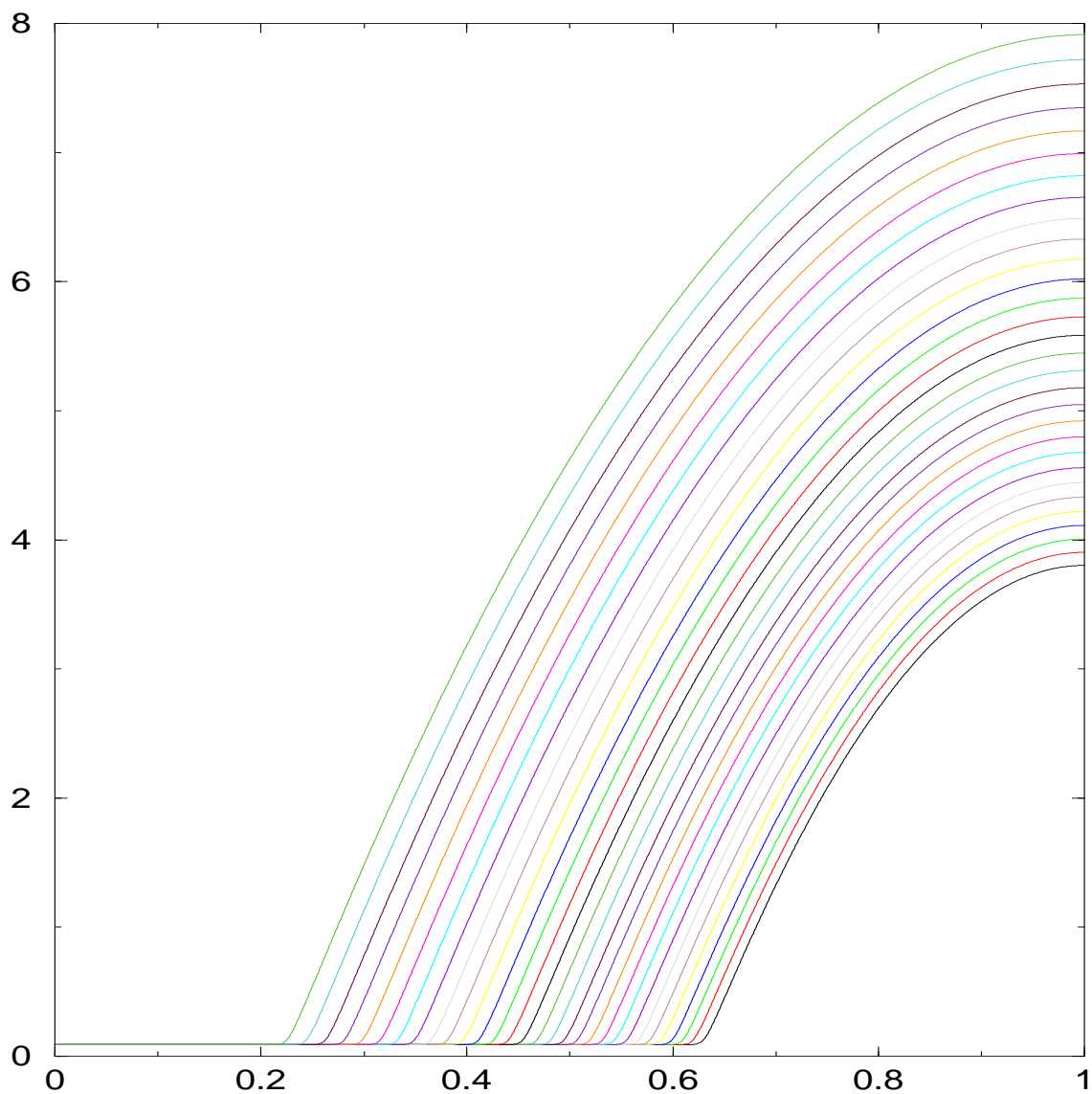Figure 2.3: Unstable solution for a=5, b=.3, L=1. Solutions are plotted for various volumes.

Figure 2.4: Droplet solution for a=5, b=.3, L=1. Solutions are plotted for various volumes. The precursor film, which covers the left-hand side of the substrate, is of thickness $\frac{3b}{2a} = .18$, and the bulk of the fluid is contained in the parabolic droplet. The droplet retains the same shape as fluid volume is increased.

Figure 6. Stable solutions on the first branch for fixed mass $\bar{u} = 1$ and values of $\epsilon = 0.2, 0.1, 0.05, 0.025, 0.0125, 0.00625$.
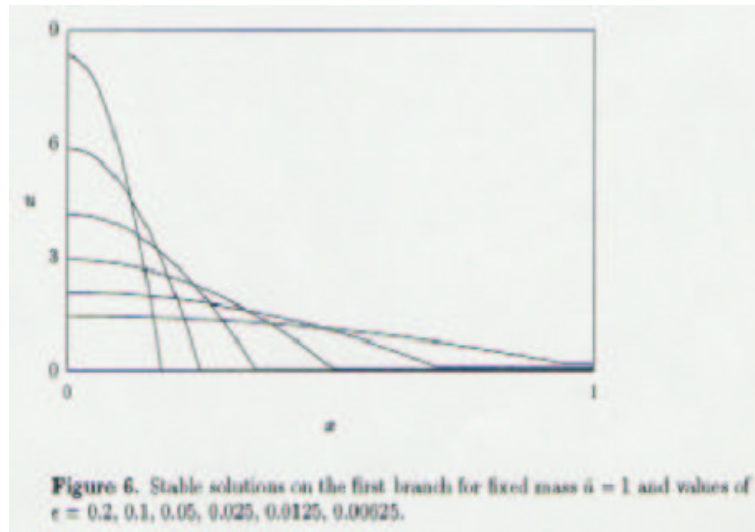
Figure 2.5: Each successively steeper droplet has had its precursor film thickness halved. As precursor film thickness approaches zero, droplet height approaches infinity- a highly nonphysical result. Figure taken from [7].

unstable energy decreases with ϵ for some perturbations $\hat{h}$ and the terms of order ϵ^2 are not strictly positive.

Integrating the first term in eq. (2.10) by parts,

$$\int_0^L \frac{\hat{h}_x^2}{2} dx = \frac{\hat{h}\hat{h}_x}{2}\bigg|_0^L - \frac{1}{2}\int_0^L \hat{h}\hat{h}_{xx}dx \tag{2.11}$$

The first term vanishes since $\hat{h}_x(0) = \hat{h}_x(L) = 0$. Substituting the second term into equation (2.10) and collecting the terms of order ϵ^2 yields

$$\int_0^L -\hat{h}\left[\frac{d^2\hat{h}}{dx^2} + \hat{h}\frac{d^2V(\bar{h})}{d\bar{h}^2}\right]dx \tag{2.12}$$

The integrand may be written as a linear operator $\mathcal{L}$ whose eigenfunctions are $cos\left(\frac{n\pi x}{L}\right)$:

$$\hat{h}\left(-\hat{h}_{xx} + \frac{d^2V(\bar{h})}{d\bar{h}^2}\hat{h}\right) = \hat{h}\mathcal{L}(\hat{h}) \tag{2.13}$$

Setting the eigenvalues $\frac{n^2\pi^2}{L^2} + \frac{d^2V(\bar{h})}{d\bar{h}^2}$ of this operator to zero yields the bifurcation condition:

$$\frac{n^2\pi^2}{L^2} + \frac{d^2}{d\bar{h}^2}\left(\frac{-a}{\bar{h}^2} + \frac{b}{\bar{h}^3}\right) = \frac{\bar{h}^5 n^2\pi^2}{L^2} - 6a\bar{h} + 12b = 0 \tag{2.14}$$

For $n = 1$, $L = 1$, $a = 5$, and $b = .3$, there are two real-valued solutions to equation (2.14) at $\bar{h} = \bar{h}_- \approx .1200$ and $\bar{h}_+ \approx 1.288$. For this set of parameters, the flat solution is stable for $\bar{h} < \bar{h}_-$, unstable for $\bar{h}_- < \bar{h} < \bar{h}_+$, and stable for $\bar{h} > \bar{h}_+$. Figure 2.6 shows the full bifurcation diagram.
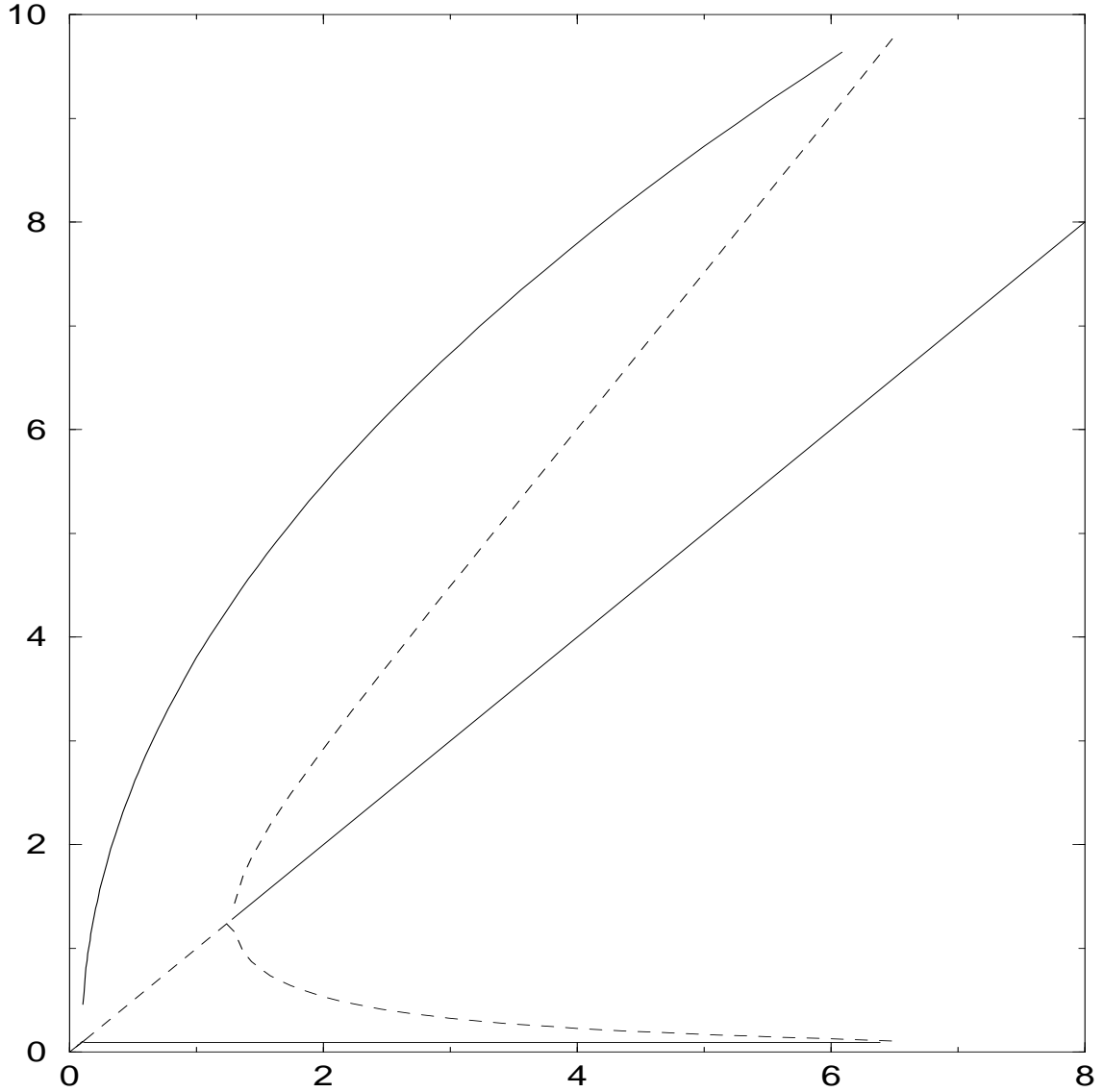
Figure 2.6: The bifurcation diagram for the lubrication model, a=5, b=.3, L=1. The x-axis is average fluid height $\bar{h}$, and the y=axis is the height $h(0)$, $h(L)$ of the fluid at each edge of the box. The higher curves show $h(L)$ at the right side of the box for each solution and the lower curves show $h(0)$ at the left; solid curves correspond to stable solutions, and dashed curves correspond to unstable solutions. The line of slope 1 corresponds to the trivial flat solution (fig. 2.2.) Note that it loses stability at $\bar{h} = \bar{h}_- \approx .1200$ and regains it at $\bar{h} = \bar{h}_+ \approx 1.288$. The stable branch which bifurcates at $\bar{h}_-$ is the droplet solution (fig. 2.4), and the unstable branch which bifurcates at $\bar{h}_+$ corresponds to fig. 2.3.

Chapter 3

Improving the model

3.1   A slight improvement

The first change we make to the lubrication model is to simply include the full differential arc length, rather than the first-order approximation, in the energy integral.

$$E = \int_0^L \sqrt{1 + h_x^2} - \frac{a}{h^2} + \frac{b}{h^3} dx \tag{3.1}$$

We find stationary interfaces using the Newton-Raphson method again; the procedure is nearly identical to that discussed in the previous section.

The stability analysis for the flat solution is also identical, since in the neighborhood of the flat solution the full arc length can indeed be approximated to first order without error. The lower bifurcation appears to be subcritical in general, but the 'corner' is difficult to trace (fig. 3.3) using this numerical method. In order to find the droplet branch (fig 3.2,) we follow the supercritical unstable branch through increasing volume until it turns around in a fold bifurcation, then perturb it strongly and decrease volume. The shape of the droplets is approximately circular rather than parabolic, as circles minimize the exact arc length.

We can now change the magnitude of the surface energy relative to the Van der Waals energy in order to see if the droplets' shape becomes steeper like the shape of the oil droplets pictured in chapter 1. Indeed, as the relative magnitude of the surface energy decreases, the droplet branch becomes steeper (fig. 3.4.) Eventually, the interface becomes nearly vertical and the method fails to converge for weaker
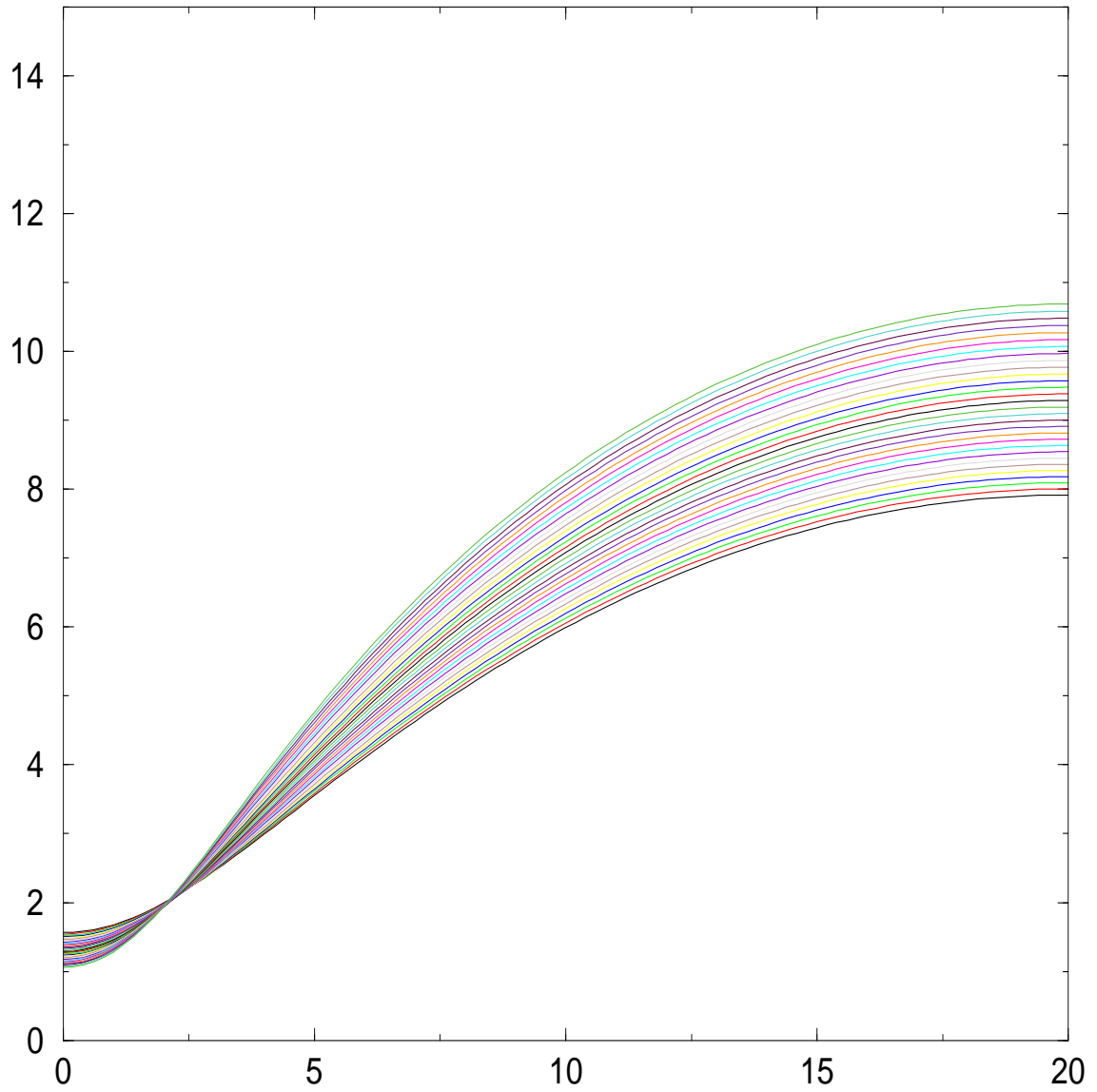
Figure 3.1: Unstable solution branch using exact arc length, $a = 1$, $b = .5$, $L = 20$. Solutions are plotted for various volumes.
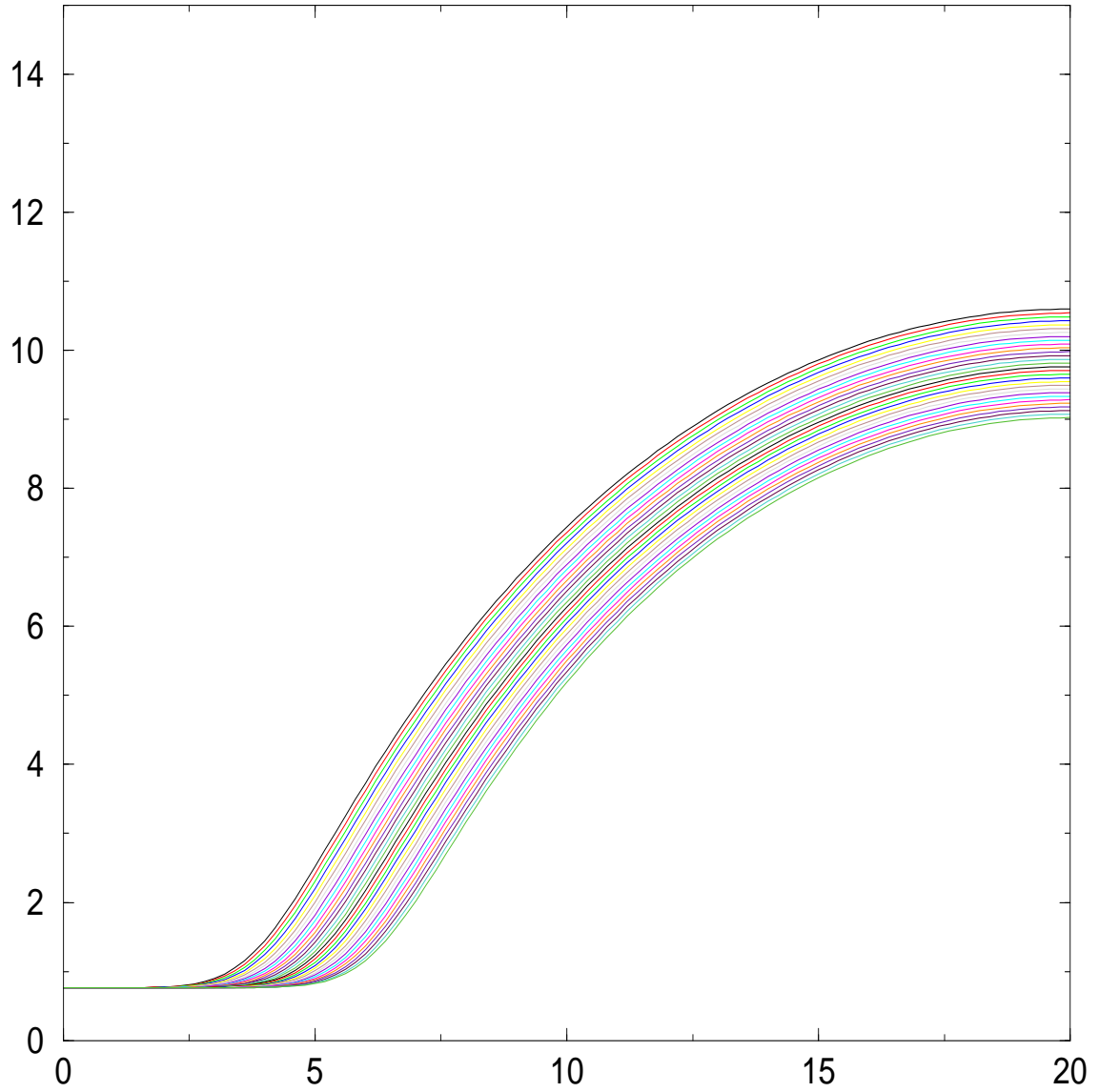
Figure 3.2: Droplet solution branch for exact arc length, $a = 1$, $b = .5$, $L = 20$. Note that the droplets are approximately circular and not parabolic. Solutions are plotted for various volumes. The depth of the precursor film is still $h_{min} = \frac{3b}{2a} = .75$.
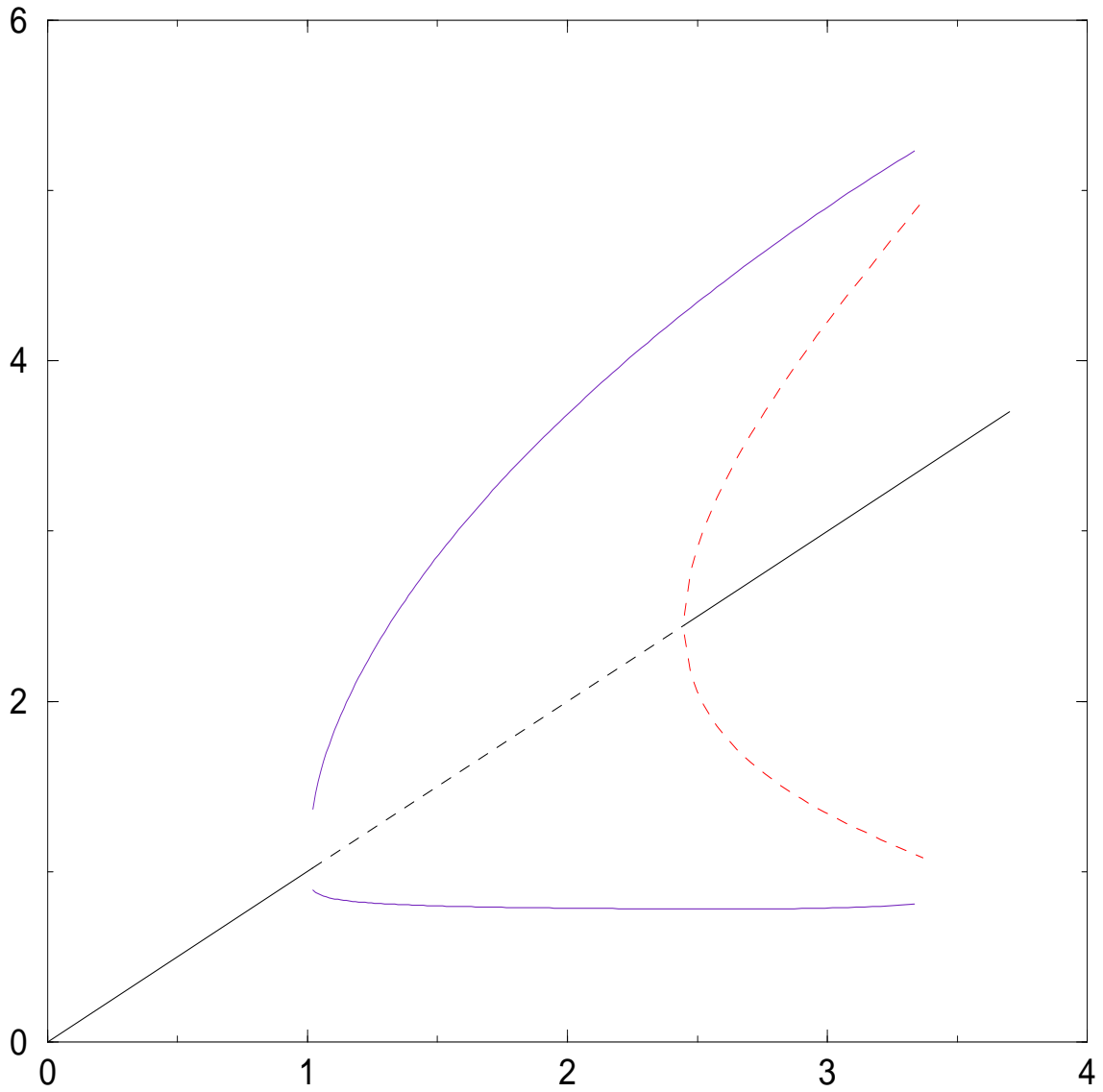
Figure 3.3: A bifurcation diagram for exact arc length, a=1, b=.5, L=20. Average interface height is plotted on the x-axis, and fluid height $h(0)$ and $h(L)$ at each side of the box is plotted on the y-axis. Solid curves correspond to stable solutions, and dashed curves correspond to unstable solutions.
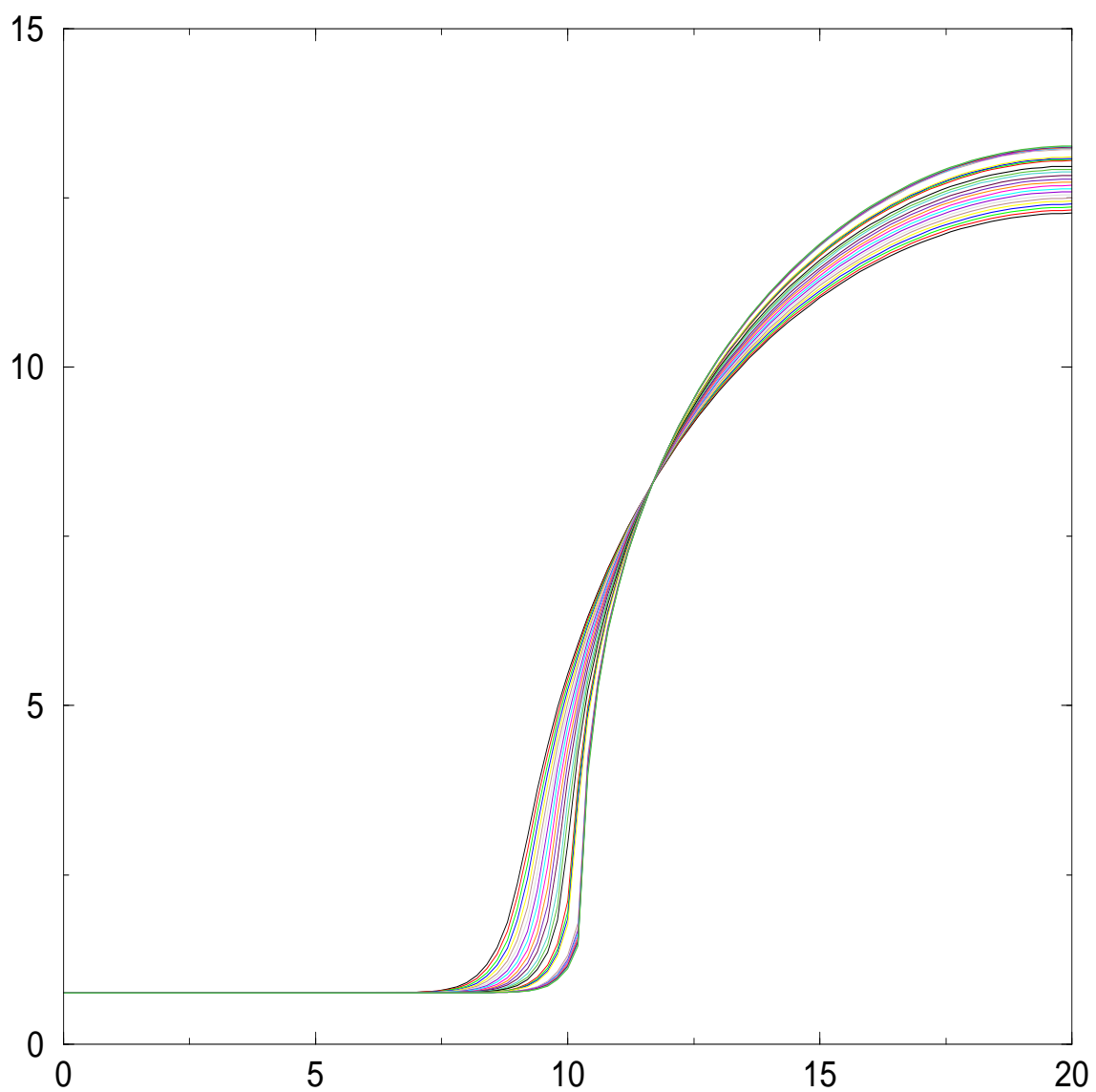
Figure 3.4: Droplet solution for a constant volume as surface energy decreases. When surface energy becomes sufficiently weak, the interface becomes nearly vertical and the method fails to converge to a stationary solution if the surface energy is weakened further.
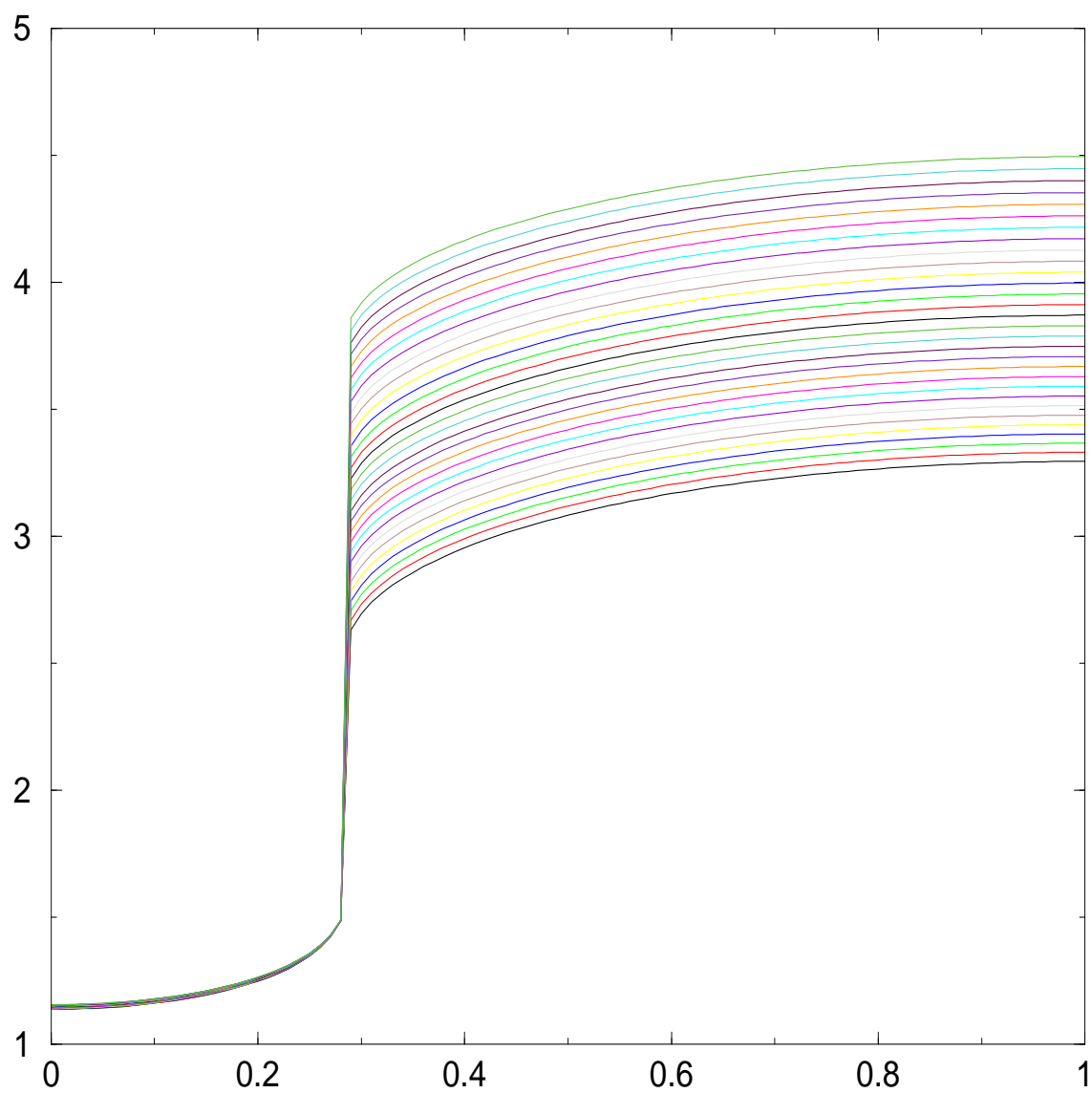
Figure 3.5: Unstable branch for various volumes at a constant, weak surface energy. The interface resembles a smooth curve that has been broken and shifted along a nearly vertical line

surface energy. The unstable branch also behaves strangely for weak surface energy (fig. 3.5;) the interface appears to be broken and shifted along a near-vertical line. Both of these behaviors suggest that for sufficiently weak surface energy the droplet branch and the unstable branch overturn; that is, $h(x)$ becomes a multivalued function of x. This numerical model, which assumes that the fluid is composed of narrow columns, is clearly unable to accomodate such solutions.

Note that the different curves in fig. 3.4 correspond to different surface energy strengths at constant volume, while the different curves in fig. 3.5 correspond to different volumes at a constant, weak surface energy. I present the data in this fashion because decreasing surface energy strength moves the high-volume bifurcation point h_+ to a higher volume. This tends to reduce the interface amplitude of the unstable solution branch as the weakening surface energy increases it, making it difficult to effectively show the strangeness of the branch's behavior on a single plot.

3.2 A major improvement

In order to allow the fluid to overturn, we parametrize the fluid interface by arc length t rather than by x. Instead of a single function $h(x)$, the arc length-parametrized interface is described by two functions $h(t)$ and $x(t)$ (fig. 3.6.)

$$E = \int_0^T \sqrt{x_t^2 + h_t^2} - \Big[\frac{a}{h(t)^2} + \frac{b}{h(t)^3}\Big] x_t \, dt \qquad (3.2)$$

When the fluid interface is discretized and represented by N points $(h_1, x_1)...(h_N, x_N)$, another numerical challenge arises; allowing each point to 'float' freely underspecifies the problem, as shifting a point along an equilibrium interface leaves energy unchanged. This can be remedied by constraining the spacing between each point to the common, but variable, length l using $N - 1$ Lagrange multipliers $k_1...k_N$:

$$E = \sum_{i=1}^{N-1} \left(l + \left(\frac{V(h_{i+1}) + V(h_i)}{2} \right)(x_{i+1} - x_i) \right.$$
$$+ k_i \left((h_{i+1} - h_i)^2 + (x_{i+1} - x_i)^2 - l^2 \right) \quad (3.3)$$
$$\left. + \lambda(x_{i+1} - x_i)\left(\frac{h_{i+1} + h_i}{2} \right) \right) - \lambda vol$$
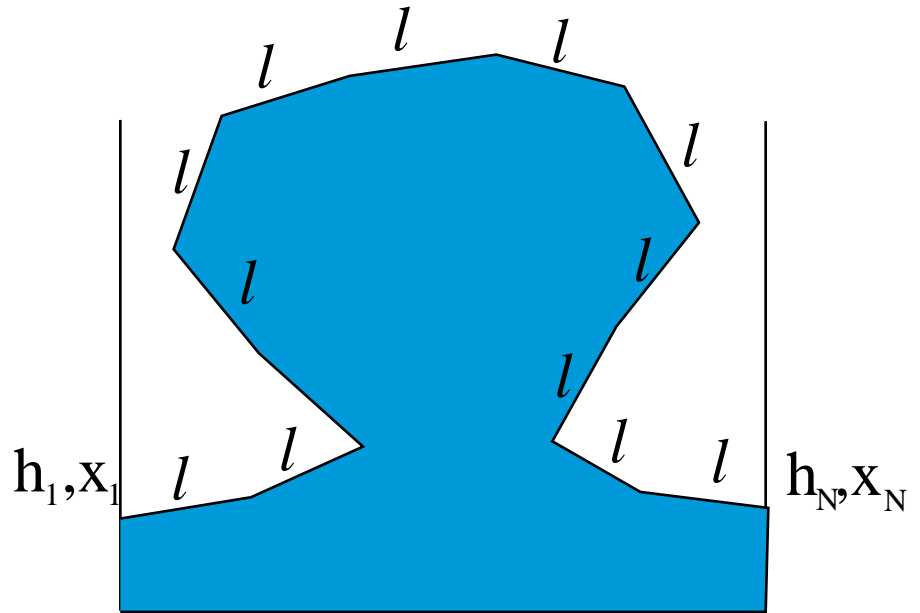
Figure 3.6: Approximating the fluid as a series of columns does not allow for overturning interfaces, but parametrizing the interface by arc length does. The spacing between each point is constrained to the common, but variable, value l.

3.3 Numerics

The problem now becomes to find values p^* of the new vector $\vec{p}$ such that the new vector $\vec{F}(\vec{p})$ is zero. We solve the problem by using the Newton- Raphson method, as before.

$$
\vec{p} = \begin{bmatrix} h_1 \\ k_1 \\ x_2 \\ h_2 \\ k_2 \\ \vdots \\ x_{N-2} \\ h_{N-2} \\ k_{N-2} \\ h_{N-1} \\ k_{N-1} \\ h_N \\ l \\ \lambda \end{bmatrix}, \vec{F}(\vec{p}) = \begin{bmatrix} \frac{\partial E}{\partial h_1} \\ \frac{\partial E}{\partial k_1} \\ \frac{\partial E}{\partial x_2} \\ \frac{\partial E}{\partial h_2} \\ \frac{\partial E}{\partial k_2} \\ \vdots \\ \frac{\partial E}{\partial x_{N-2}} \\ \frac{\partial E}{\partial h_{N-2}} \\ \frac{\partial E}{\partial k_{N-2}} \\ \frac{\partial E}{\partial h_{N-1}} \\ \frac{\partial E}{\partial k_{N-1}} \\ \frac{\partial E}{\partial h_N} \\ \frac{\partial E}{\partial l} \\ \frac{\partial E}{\partial \lambda} \end{bmatrix}
\tag{3.4}
$$

The Jacobian matrix $J(\vec{p})$, which I have not shown due to its size, is expanded to include mixed partial derivatives with respect to the new parameters $\vec{x}$, $\vec{k}$, and l. The x coordinates of the boundary points, x_1 and x_N, are not allowed to change; if they were, translating the solution along the x axis would leave the energy unchanged and the Jacobian would become singular, rendering the Newton-Raphson method useless.

The linear stability analysis for the flat solution is still the same as in chapter 2, but in order to extract matching stability information from the numerical code we must take another step. The Jacobian matrix is the discretized equivalent of the

linear operator $\mathcal{L}$ in equation (2.13,) but the Jacobian's eigenvalues v_j and eigenvectors $\hat{p}_j$, which are composed of $\hat{h}_{j,i=1..N}$, $\hat{x}_{j,i=2..N-1}$, $\hat{k}_{j,i=1..N-1}$, $\hat{l}_j$, and $\hat{\lambda}_j$, obey the eigenvalue equation

$$J\hat{p}_j = v_j\hat{p}_j \tag{3.5}$$

These do not necessarily correspond to eigenvectors and eigenvalues of $\mathcal{L}$, as the derivation of $\mathcal{L}$ assumes that all perturbations obey the same constraints and boundary conditions as the solutions they perturb. In order to obtain the correct eigenvalues and eigenvectors from the numerical code, the Jacobian's eigenvectors must be forced to obey the constraints:

$$\hat{k}_{j,i}\big((\hat{h}_{j,i+1} - \hat{h}_{j,i})^2 + (\hat{x}_{j,i+1} - \hat{x}_{j,i})^2 - \hat{l}_j^2\big) = 0$$
$$\hat{\lambda}_j\Big(\frac{\hat{h}_{j,i+1} + \hat{h}_{j,i}}{2}\Big) - \hat{\lambda}_j vol = 0 \tag{3.6}$$

The first derivative of the energy of a perturbed fluid interface $\frac{dE(p^*+\epsilon\hat{p}_j)}{dc^m}\big|_{c_m=c_m^*}$ with respect to c_m^*, which is one of the constraint parameters $k_{1..N}^*, \lambda^*$ corresponding to the stationary solution p^*, can be expanded to give

$$\frac{\partial E(p^* + \epsilon\hat{p}_j)}{\partial c^m}\bigg|_{c_m=c_m^*} = \frac{\partial E(p^*)}{\partial c^m}\bigg|_{c_m=c_m^*} + \epsilon\hat{p}_j\Big(\frac{\partial^2 E(p^*)}{\partial p_1 \partial c_m} + ...\Big)\bigg|_{c_m=c_m^*,\vec{p}=p^*} + O(\epsilon^2) \tag{3.7}$$

The first term is equal to zero for stationary solutions, and the term of order ϵ contains the contribution of the perturbation to the constraint energy up to the order of the second variation of the energy. This term is simply the perturbing vector $\hat{p}$ multiplied by the row of the Jacobian that contains the mixed partial derivatives involving c_m. In order to force the eigenvectors of the Jacobian to obey the constraints, therefore, it is necessary to use the modified eigenvalue equation

$$J(p^*)\hat{p}_j = v_j B\hat{p}_j \tag{3.8}$$

where B is an identity matrix of the same size as the Jacobian with diagonal elements whose indices corresponding to constraint parameters have been zeroed:

$$
\vec{p} =
\begin{bmatrix}
h_1 \\
k_1 \\
x_2 \\
h_2 \\
k_2 \\
\vdots \\
x_N - 2 \\
h_N - 2 \\
k_N - 2 \\
h_N - 1 \\
k_N - 1 \\
h_N \\
l \\
\lambda
\end{bmatrix}
, B =
\begin{bmatrix}
1 & 0 & 0 & 0 & 0 & \cdots & 0 & 0 & 0 & 0 & 0 & 0 & 0 & 0 \\
0 & 0 & 0 & 0 & 0 & \cdots & 0 & 0 & 0 & 0 & 0 & 0 & 0 & 0 \\
0 & 0 & 1 & 0 & 0 & \cdots & 0 & 0 & 0 & 0 & 0 & 0 & 0 & 0 \\
0 & 0 & 0 & 1 & 0 & \cdots & 0 & 0 & 0 & 0 & 0 & 0 & 0 & 0 \\
0 & 0 & 0 & 0 & 0 & \cdots & 0 & 0 & 0 & 0 & 0 & 0 & 0 & 0 \\
\vdots & \vdots & \vdots & \vdots & \vdots & \ddots & \vdots & \vdots & \vdots & \vdots & \vdots & \vdots & \vdots & \vdots \\
0 & 0 & 0 & 0 & 0 & \cdots & 1 & 0 & 0 & 0 & 0 & 0 & 0 & 0 \\
0 & 0 & 0 & 0 & 0 & \cdots & 0 & 1 & 0 & 0 & 0 & 0 & 0 & 0 \\
0 & 0 & 0 & 0 & 0 & \cdots & 0 & 0 & 0 & 0 & 0 & 0 & 0 & 0 \\
0 & 0 & 0 & 0 & 0 & \cdots & 0 & 0 & 0 & 1 & 0 & 0 & 0 & 0 \\
0 & 0 & 0 & 0 & 0 & \cdots & 0 & 0 & 0 & 0 & 0 & 0 & 0 & 0 \\
0 & 0 & 0 & 0 & 0 & \cdots & 0 & 0 & 0 & 0 & 0 & 1 & 0 & 0 \\
0 & 0 & 0 & 0 & 0 & \cdots & 0 & 0 & 0 & 0 & 0 & 0 & 1 & 0 \\
0 & 0 & 0 & 0 & 0 & \cdots & 0 & 0 & 0 & 0 & 0 & 0 & 0 & 0
\end{bmatrix}
\tag{3.9}
$$

The eigenvalues and eigenvectors of the stability operator $\mathcal{L}$ for a flat interface of height $\bar{h}$ in a box of length L parametrized using N gridpoints are

$$
\hat{h}(x) = \cos\left(\frac{n\pi x}{L}\right) \Rightarrow \hat{x}_{j,i} \approx (i-1)\frac{L}{N-1}, \hat{h}_{j,i} = \cos\left(\frac{j\pi\hat{x}_{j,i}}{L}\right)
$$
$$
v_j = \frac{\bar{h}^5 j^2 \pi^2}{L^2} - 6a\bar{h} + 12b
\tag{3.10}
$$

The numerical eigenvalues and some samples of the h components of the eigenvectors of equation (3.8) for $\bar{h} = 2$, $L=20$, $N = 51$, $a = 1$, $b = .5$ are shown in figures 3.7, 3.8, and 3.9, respectively. The eigenvalues corresponding to small values of j in equations (3.10) agree with theory up to a factor of $N+2$; we're not sure where this factor comes from, but we hope to find it soon and at any rate it doesn't change the

locations of the bifurcation points. The eigenvalues corresponding to higher values of j deviate from the predicted parabolic spectrum because the higher-frequency eigenvectors cannot be accurately represented due to the finite number of points available.
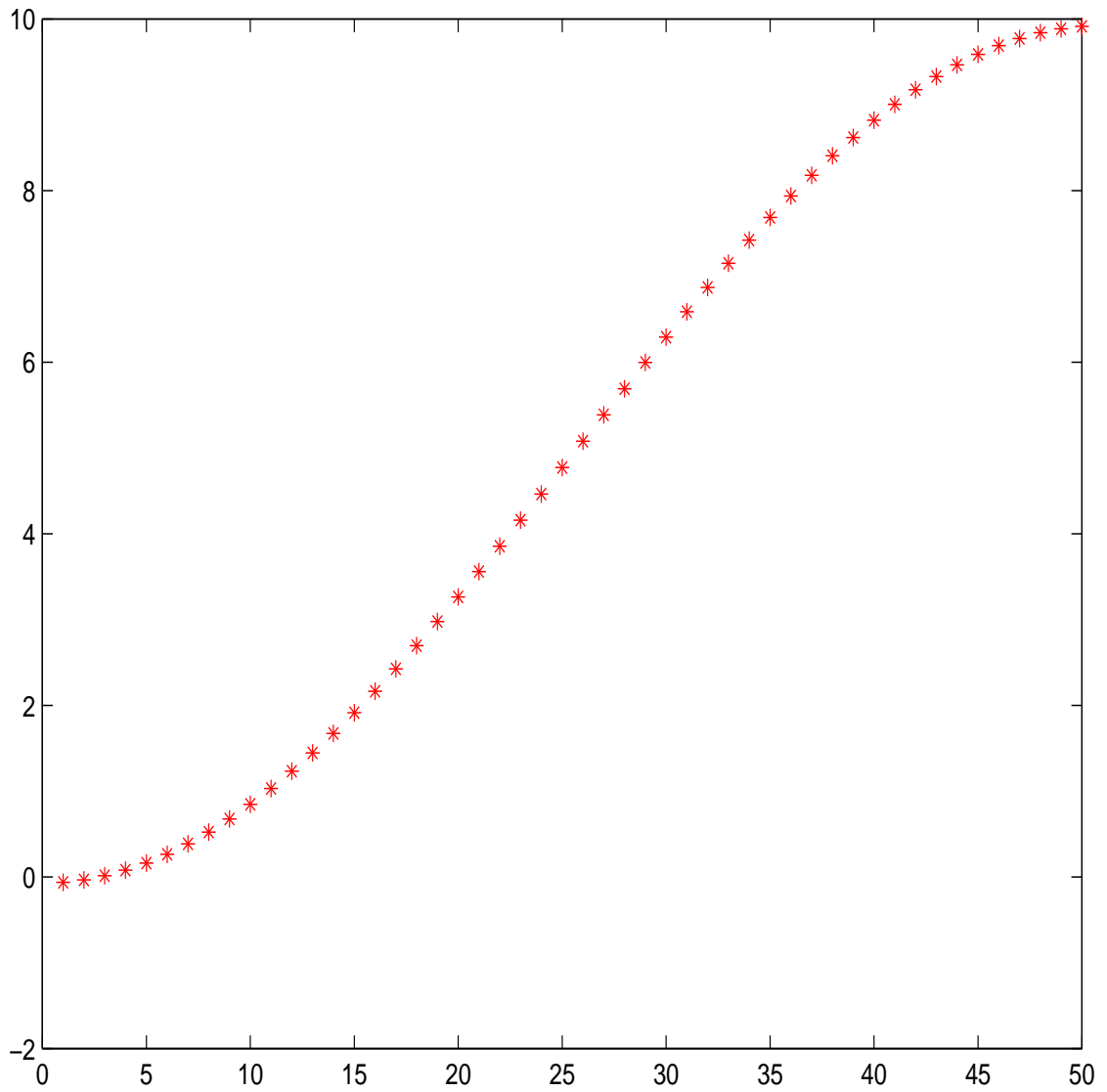
Figure 3.7: The eigenvalue spectrum is accurate up to a factor of $N + 2$ for low-frequency eigenvectors. Each constraint-obeying eigenvalue v_j of the Jacobian is plotted against its index j.
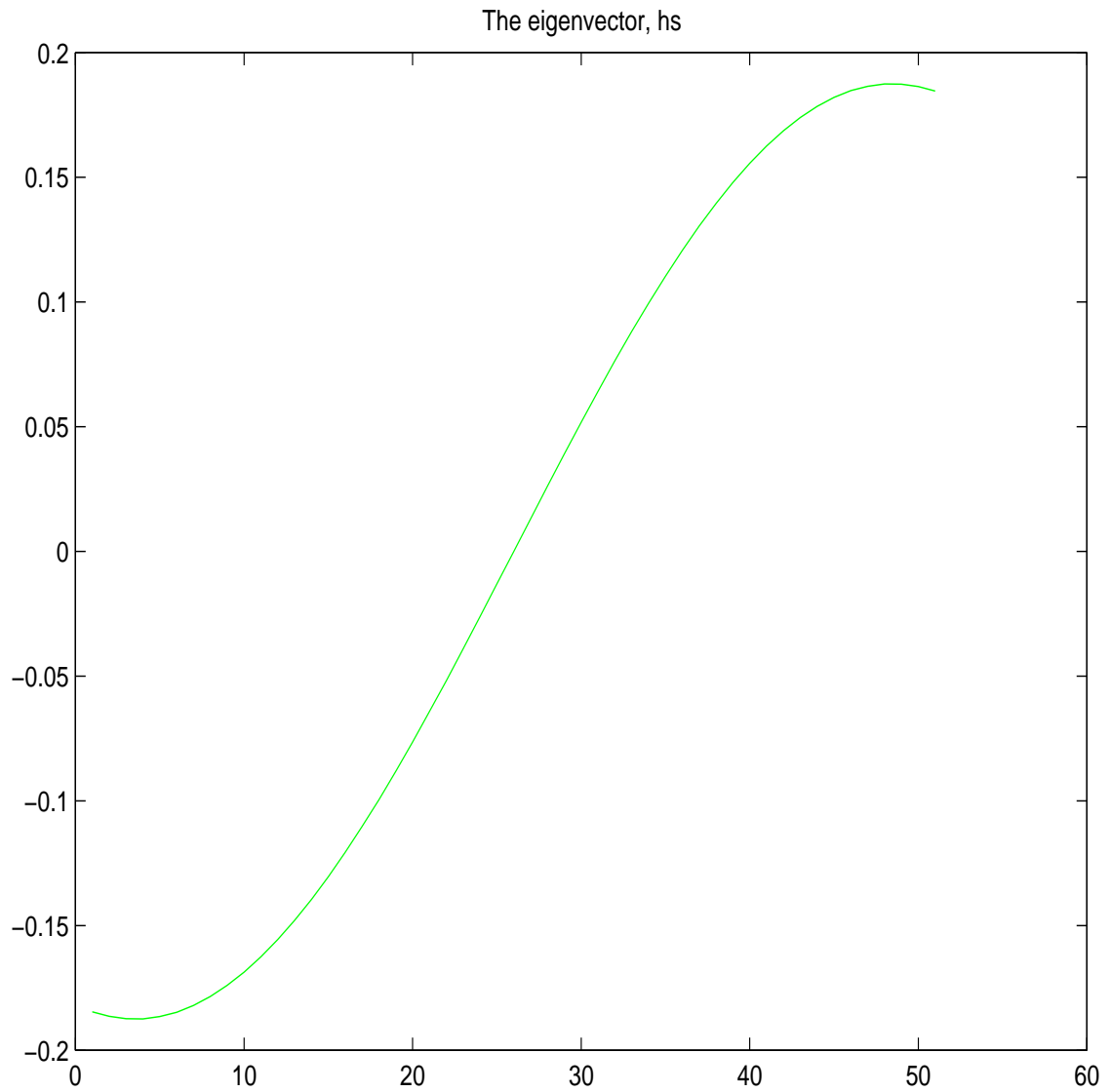
Figure 3.8: The low-frequency eigenvectors are cosines, as predicted. The h components $\hat{h}_{1,i=1..N}$ are plotted against their indices i. The eigenvectors appear to have nonzero slope at the boundaries because Matlab has ininterpolated $\hat{h}_{1,i=1..N}$ using cubic splines.

Figure 3.9: The eigenvalue spectrum deviates from theory for high-frequency eigenvectors because these eigenvectors cannot be accurately represented due to the finite grid size. The h components $\hat{h}_{j,i=1..N}$ of the eigenvector are plotted against their indices i.

Chapter 4

Results and conclusion

4.1   Qualitative results

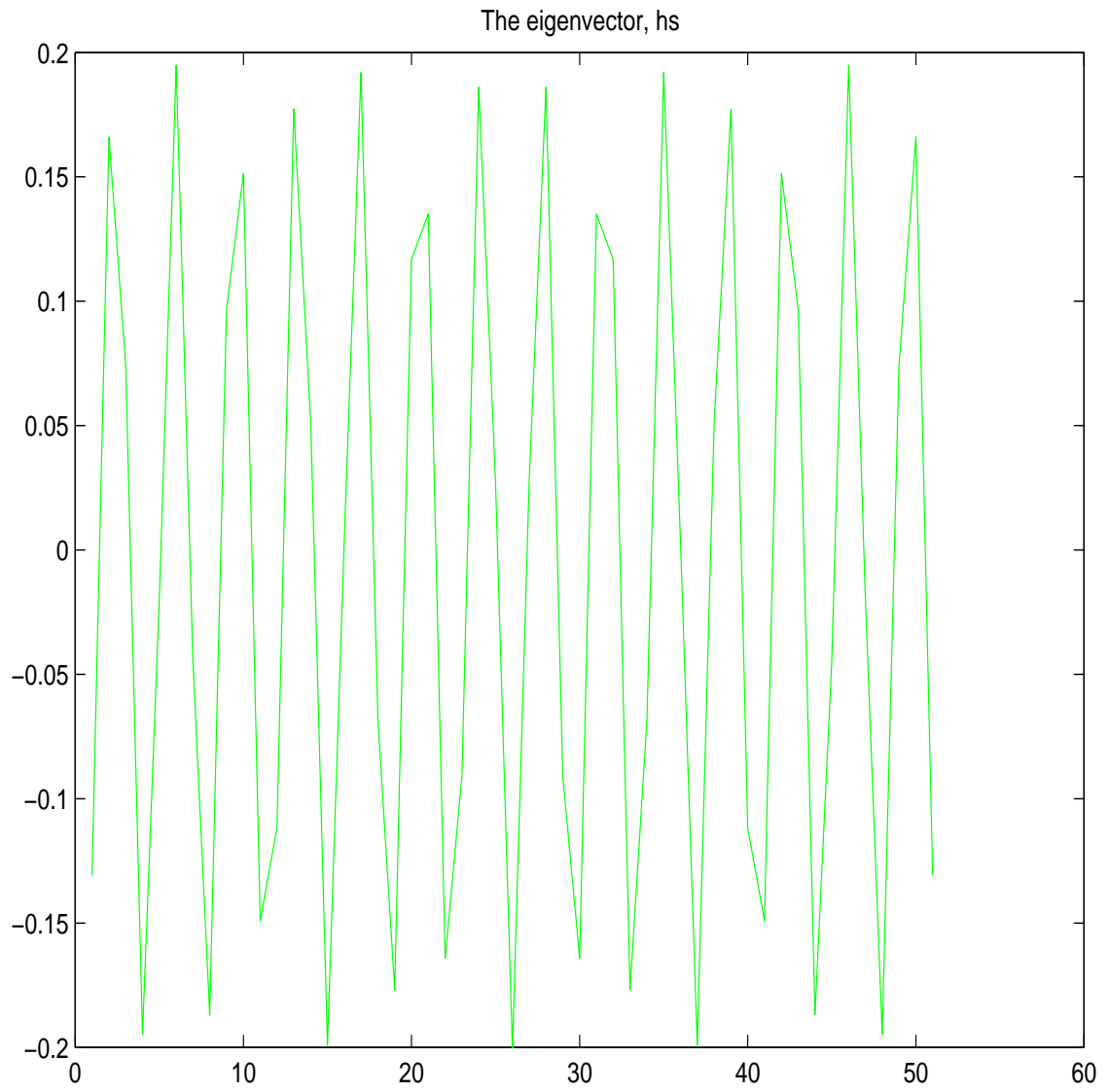After checking to make sure that the arc length-parametrized code agrees with the x-parametrized code for values of a, b, and L which do not give rise to any overturning solution branches (a typical bifurcation diagram and the stability of the constituent branches are plotted in figs. 4.1 and 4.2, respectively,) we begin to use the arc length- parametrized code to explore solution branches and parameter ranges which have been inaccessible until now.

For appropriate choices of a, b, and L, all three non-flat solution branches can overturn (the subcritical bifurcation from the flat solution is traceable using arc length parametrization.) Figs. 4.3, 4.4, and 4.5 are examples of the strange and beautiful plots that can result when the subcritical unstable branch, the droplet branch, and the supercritical unstable branch, respectively, are made to overturn. Note that these three plots are not related to each other. They were generated using different initial parameters, and the droplet branch is plotted at constant volume and various surface energy strengths while the unstable branches are plotted at constant surface energy strength and various volumes for the reason discussed in section 3.1.

The droplet solution approximates a portion of a circle sitting on a precursor film whose depth is equal to the equilibrium depth h_{min} of the Van der Waals potential. The two parts of the solution are smoothly connected by a 'foot,' which is a subject of further research interest. If the magnitudes of the energy terms are
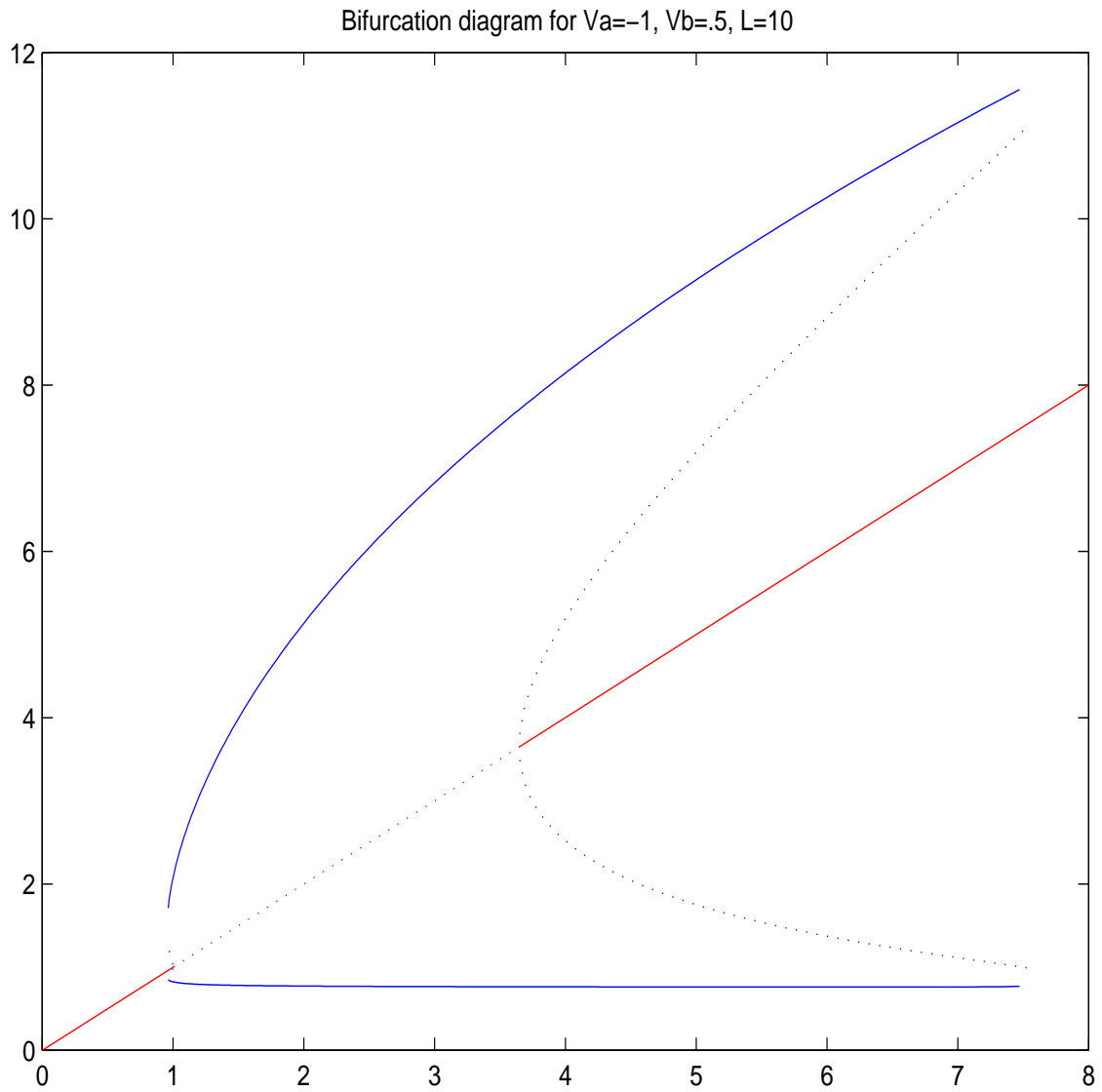
Figure 4.1: A bifurcation diagram for the arc length parametrized code, $a = 1$, $b = .5$, $L = 10$. The Average fluid height is plotted on the x-axis, and the heights $h(0)$ and $h(L)$ of the stationary interfaces at the edges of the box are plotted along the y-axis. Solid lines correspond to stable solutions, and dashed lines correspond to unstable solutions.
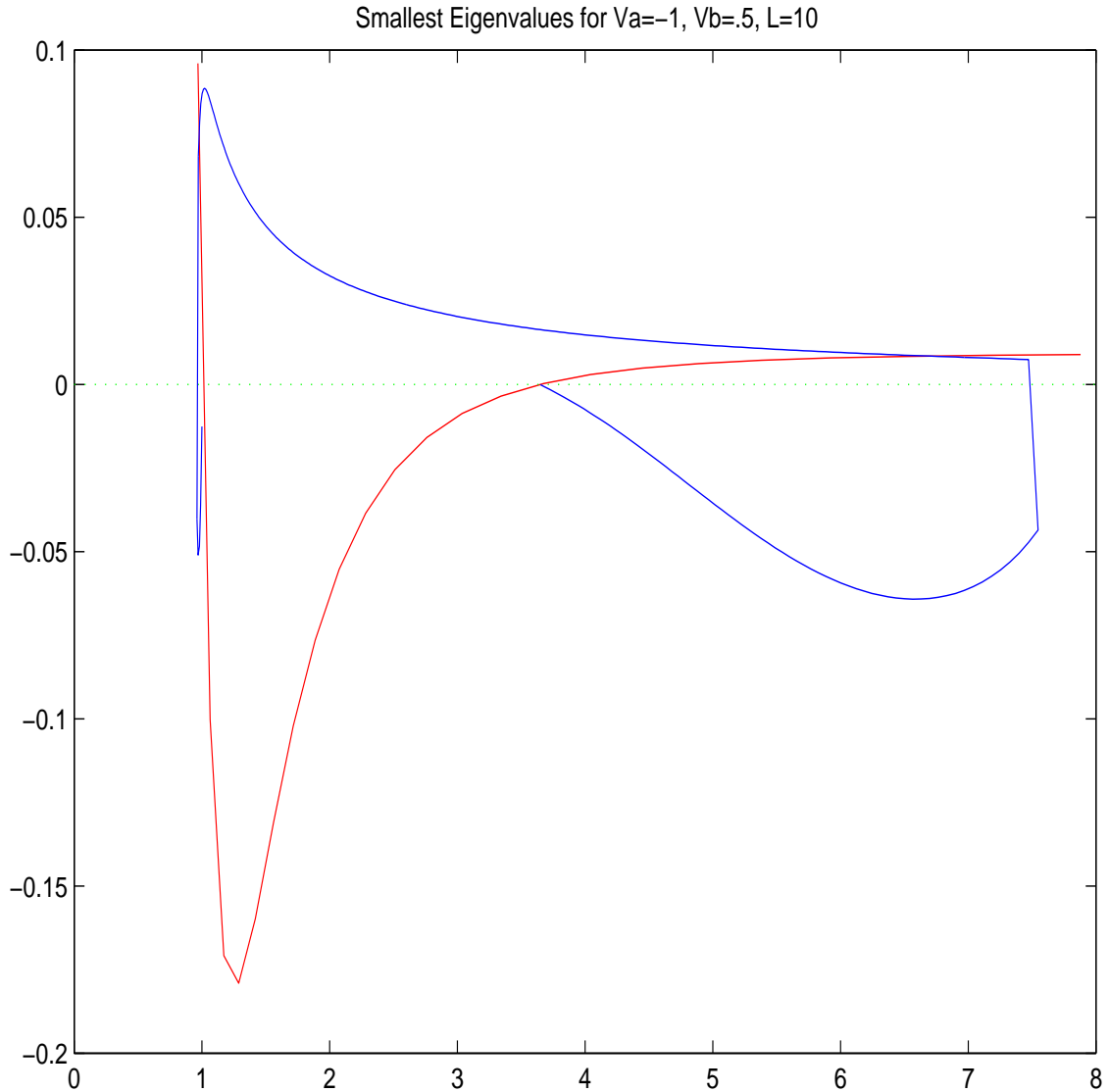
Figure 4.2: The smallest eigenvalue of the Jacobian matrix for the four solution branches. The stability of the droplet solution and the unstable branches that connect it subcritically and super-critically to the flat solution are plotted in blue, and the flat solution is plotted in red. Average fluid height $\bar{h}$ is plotted on the x-axis. The flat solution is stable for low $\bar{h}$, but it becomes unstable at the first bifurcation point, $\bar{h}_{-} \approx 1.00$. The subcritical unstable branch becomes more unstable with decreasing volume, then folds into the droplet branch, which becomes gradually less stable as volume increases. The droplet branch eventually folds into the supercritical unstable branch, which becomes an equilibrium solution when the droplet regains its stability at $\bar{h}_{+} \approx 3.65$.

Figure 4.3: The unstable branch that connects the droplet branch subcritically to the flat solution overturning. This plot was generated using $a = 100$, $b = 53$, and $L = 1$, and steeper solutions correspond to lower volume.

Figure 4.4: The droplet branch overturning for $L = 20$, $\bar{h} = 3.65$, and a and b decreasing from 1 and .5, respectively. Steeper solutions correspond to weaker surface energy.
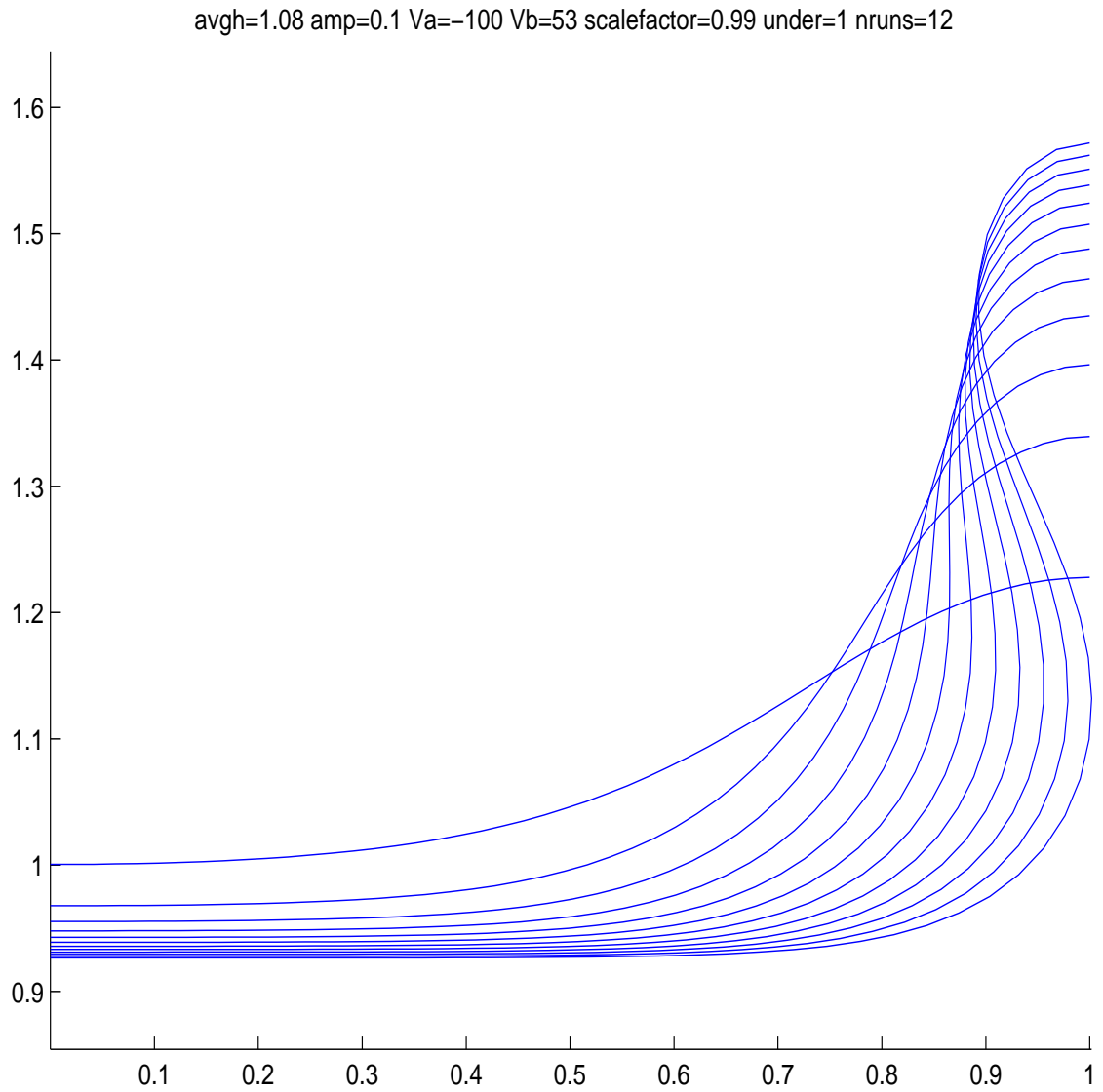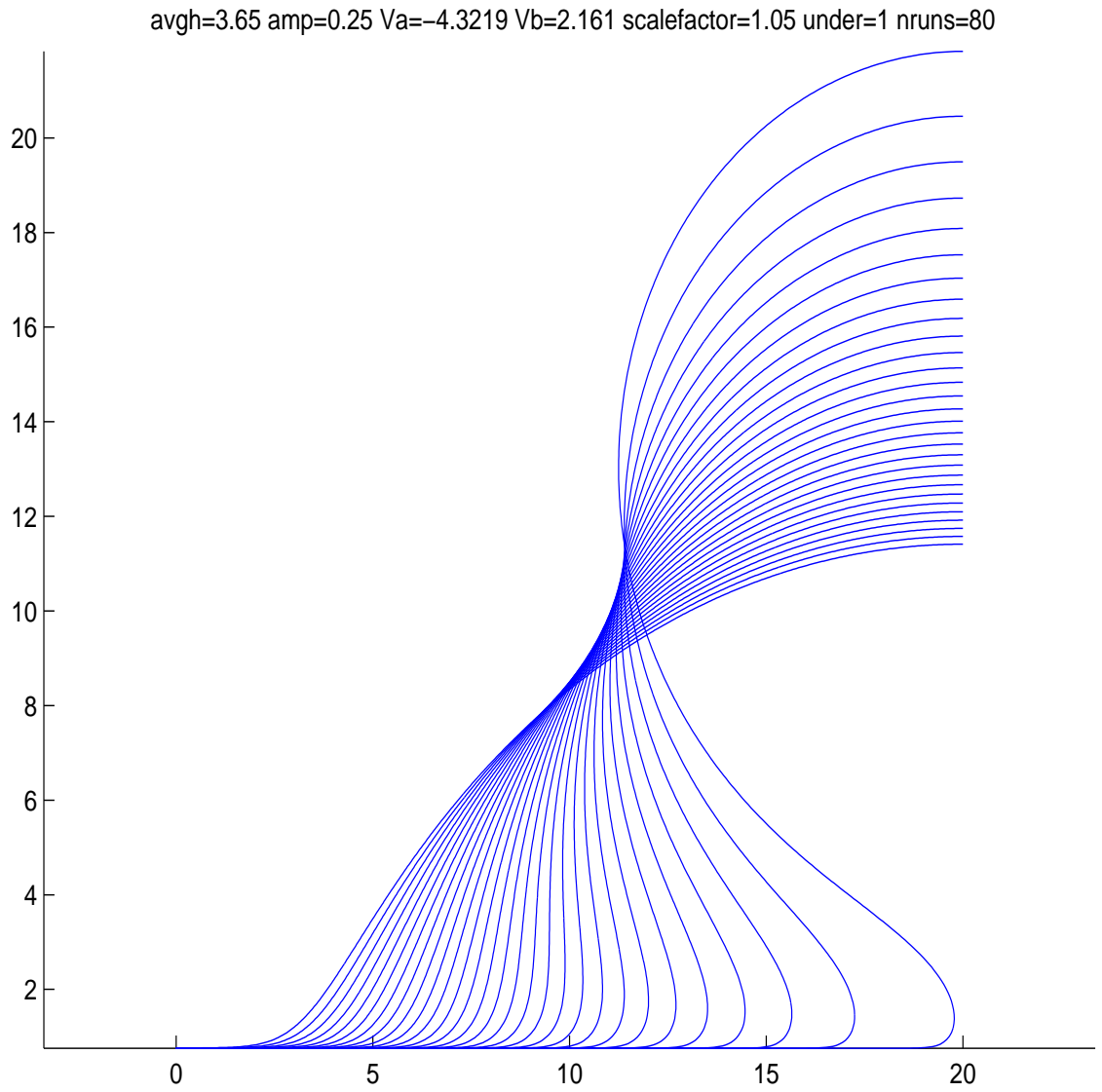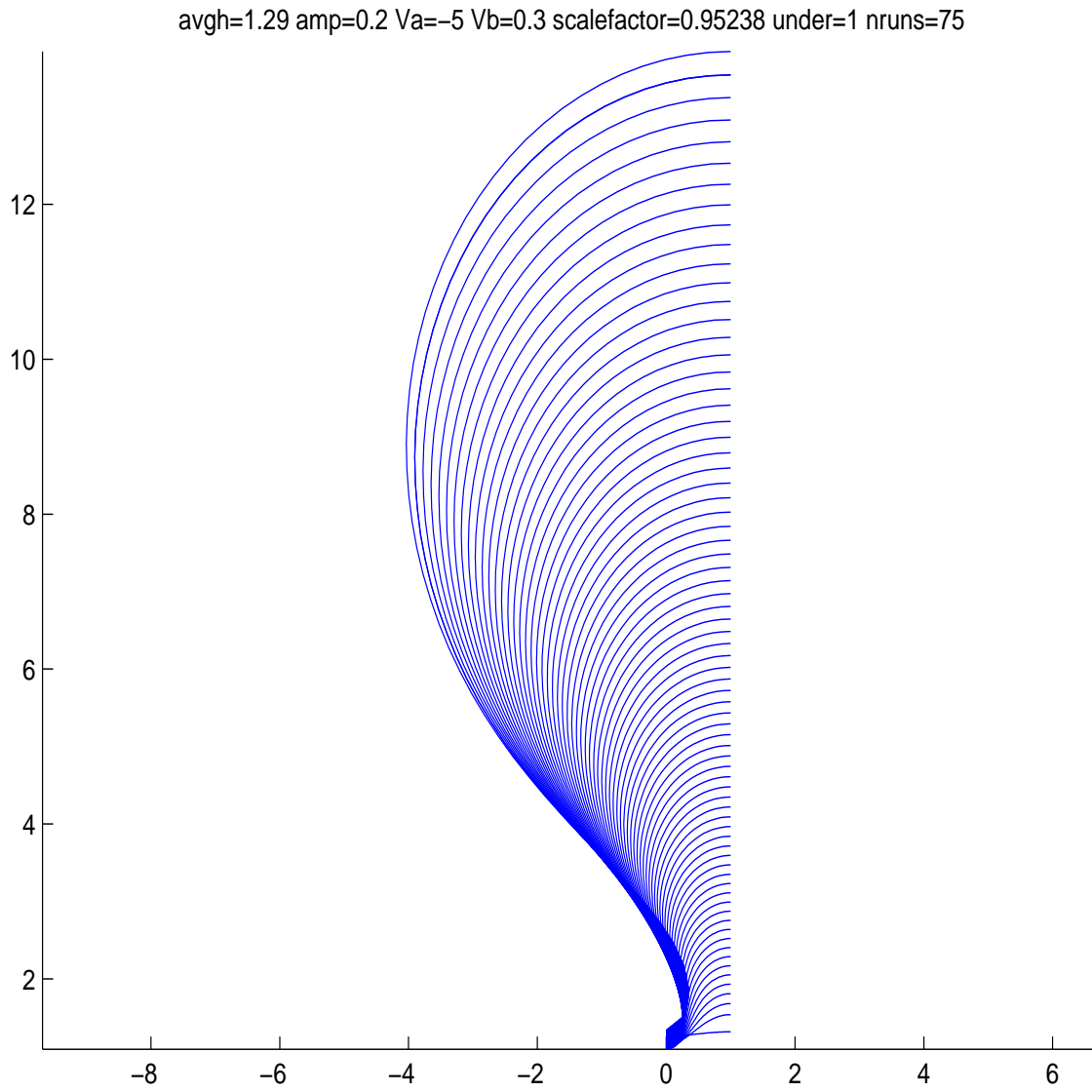
Figure 4.5: The unstable branch that connects the droplet branch subcritically to the flat solution overturning. This plot was generated using a=5, b=.3, and L=1, and larger solutions correspond to higher volume.

held constant and the volume of the film is increased, the droplet tends to keep its shape, and in particular the slope of the interface at the base of the droplet does not change appreciably, but the circular portion increases in size (fig. 3.2.) The droplet branch is stable as volume increases until the droplet foot encounters the wall of the box, at which point it merges with the supercritically bifurcated unstable solution.

If the surface energy is decreased (or, equivalently, if both Van der Waals terms are increased) (fig. 4.4,) the droplet pulls away from the surface and its foot is drawn inward (making the droplet stable over a greater range of volume.) The points at the droplet foot tend to become sparse relative to the foot's high curvature for overturning droplets, making it numerically difficult to follow the droplet branch to very weak surface energies. It is also extremely difficult to 'round corners' of the bifurcation diagram when the solutions overturn; so far, we have only been able to overturn the droplet branch by finding a relatively flat droplet and then following it through decreasing surface energy.

4.2 Quantitative results

In order to quantify these observations of the droplet branch, we need a measure of the 'pulled-awayedness' of the droplet from the surface. One such measure that is very often used in analysis of droplets that sit on a completely dry surface is contact angle (fig. 4.6) [18], but the droplets produced by our model are smoothly connected to the precursor film in such a way that the slope of the interface is continuous everywhere; the interface never actually contacts the substrate, nor does it ever make a sharp contact angle with the precursor film. After observing that the interface at the droplet foot is concave up while the interface of the droplet itself is concave down, we define the contact angle θ of the droplet as the angle that the tangent to the interface makes with the horizontal directly above the inflection

point between foot and droplet (figure 4.7.) The reason for this choice of contact angle is that it seems to be just above the droplet foot, and just at the base of the droplet proper.

Young's Law is a famous result governing the contact angle that droplet interfaces make with otherwise dry substrates:

$$1 - \cos(\theta) = \frac{W}{E_{surface}} \qquad (4.1)$$

where θ is the contact angle and W is the adhesion energy per unit area between fluid and substrate [18]. Our model certainly preserves equation (4.1)'s y-intercept; if the surface energy is strong enough, the flat solution never loses its stability and the contact angle is π for all fluid volumes. Figure 4.8 shows the relationship between $\cos(\theta)$ and $\frac{1}{E_{surface}}$. The relationship is approximately linear to well past the point of overturning; the slope of the fitline is $-.3982$, and the y-intercept is 1.0646. We have not been able to explain the slope of the line analytically, but the small deviation of the y- intercept from 1 is to be expected. The relationship appears to be very slightly concave down, and we know that the near-linear relationship cannot hold for all surface energies, since the surface energy required to keep the flat solution stable for all volumes is finite. The relationship between $\cos(\theta)$ and $\frac{1}{E_{s}urface}$ will deviate strongly from linear as surface energy approaches this critical value, since the droplet branch in this regime will tend to be very long and shallow. When the droplet interface becomes low, the Van der Waals potential has a significant effect on the shape of the bulk of the droplet. In other words, the droplet becomes 'all foot' rather than a well-defined circular droplet connected by a small foot to a well- defined precursor film, and small increases in droplet height due to relaxing surface energy will sharply decrease the Van der Waals forces at the interface. When surface energy is greater than the critical value, the relationship plotted in fig. 4.8 becomes horizontal, since the flat solution is the only equilibrium solution.

One of the major motivations for developing this model was the lubrication
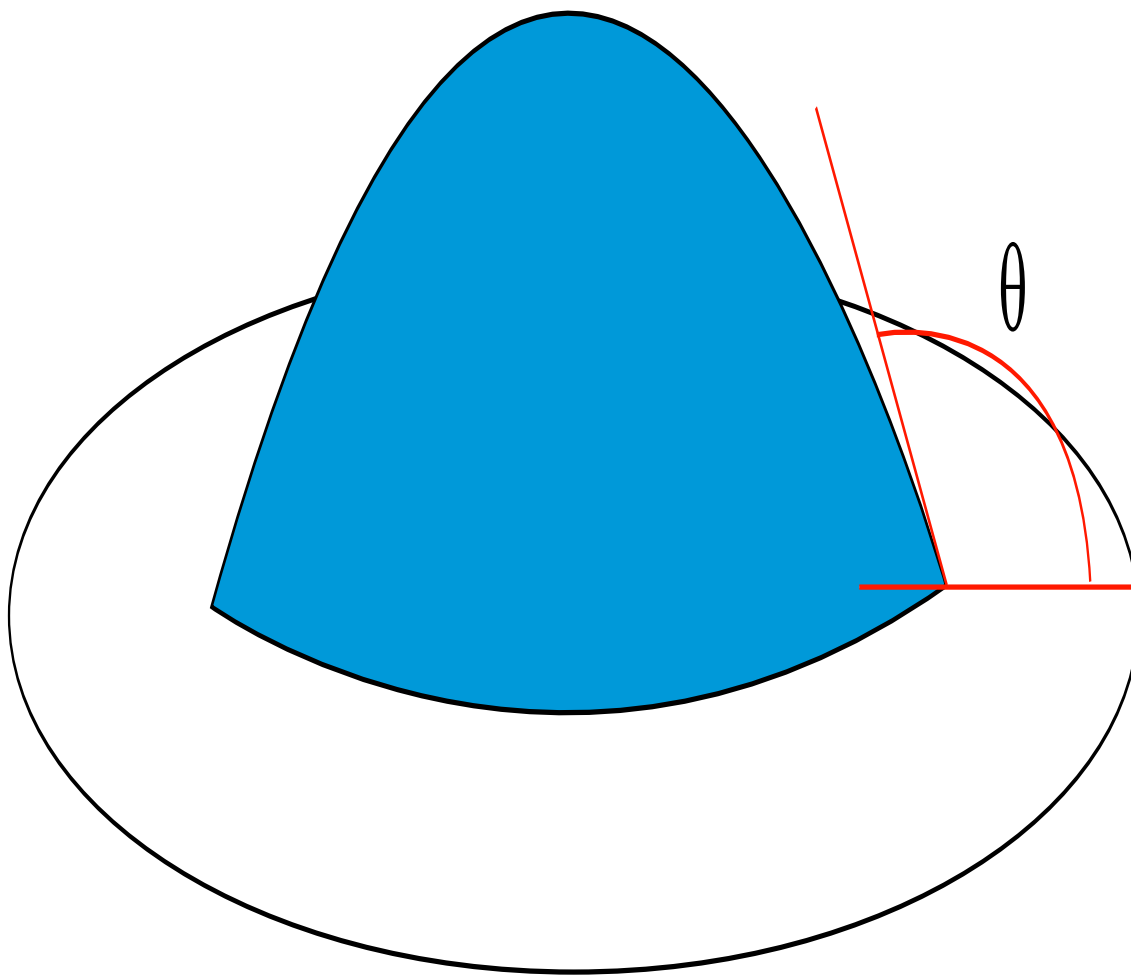
Figure 4.6: The contact angle of a droplet is the angle that its surface makes with the substrate at the droplet base. Droplets that sit on a precursor film have no such contact angle.

Figure 4.7: We define the contact angle as the angle that the droplet surface makes with the horizontal at the inflection point between the droplet's foot and the rest of the droplet. Our intent is to measure the angle of the interface just above the boundary layer where the Van der Waals energy and the surface energy commingle.

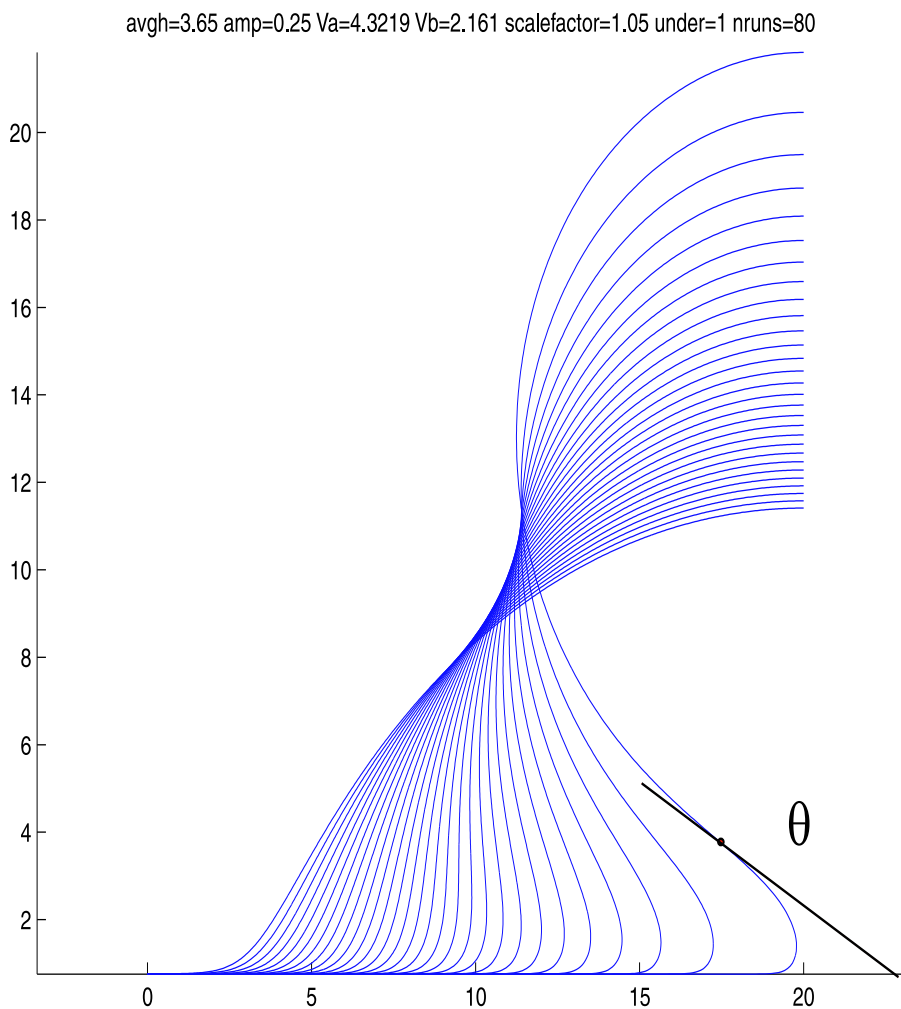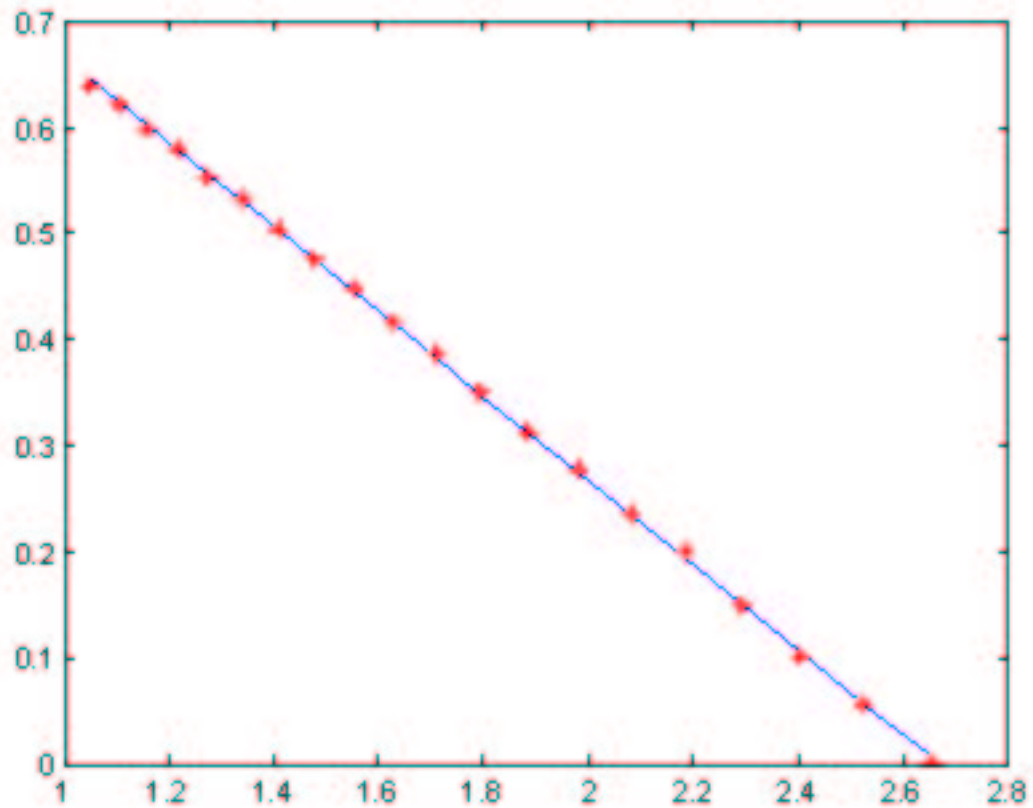Figure 4.8: The cosine of the contact angle is plotted on the y-axis, and $\frac{1}{E_{surface}}$ is plotted along the x-axis for $a = 1$, $b = .5$, and $L = 20$. The slope of the fitline is $-.3982$, and the y-intercept is 1.0646 It is somewhat surprising that the y-intercept should be anything other than 1 exactly, since if surface energy is sufficiently high the flat solution never loses stability. The relationship appears very slightly concave down, and we expect a strong deviation from linear for very strong surface energy.

model's prediction that droplet height approaches infinity as the precursor film depth is reduced. In order to see whether this model remedies that problem, we investigate the behavior of the droplet profiles for progressively shallower precursor films. We drive precursor depth down by reducing b, the repulsive term in the Van der Waals potential. Figure 4.9 shows droplet profiles as b is reduced, and figure 4.10 shows the relationship between droplet height and $\frac{1}{h_{min}} = \frac{2a}{3b}$. Like the lubrication model, this model appears to predict that droplet height approaches infinity as h_{min} approaches zero. However, the droplet's foot penetrates the right-hand sidewall! The droplet has pinched off and separated from the precursor film, much like the oil droplets pictured in chapter 1. This prediction is far more physically believable than droplets whose height increases without bound.

4.3   Conclusion

Our attempt to model overturning droplets has been a success. We have found that Van der Waals forces between a thin fluid film and the substrate it sits on and surface interaction between the film and a surrounding fluid can cause the film to break up into droplets sitting on a very thin precursor film. The depth of this precursor film minimizes the precursor film-substrate Van der Waals energy, and the droplet tends to take on a circular shape, which minimizes surface energy. The droplet and precursor film are connected by a smooth 'foot,' a boundary layer where the Van der Waals energy and surface interaction energy are of comparable magnitude. If the surface interaction is sufficiently weak the droplet can overturn and eventually pinch off from its precursor film. The cosine of the angle that the droplet interface at the inflection point between foot and droplet makes with the vertical is roughly inversely proportional to the magnitude of the surface interaction if the magnitude of the surface interaction is sufficiently small. For very strong surface interactions we expect a deviation from this near-linear rela-
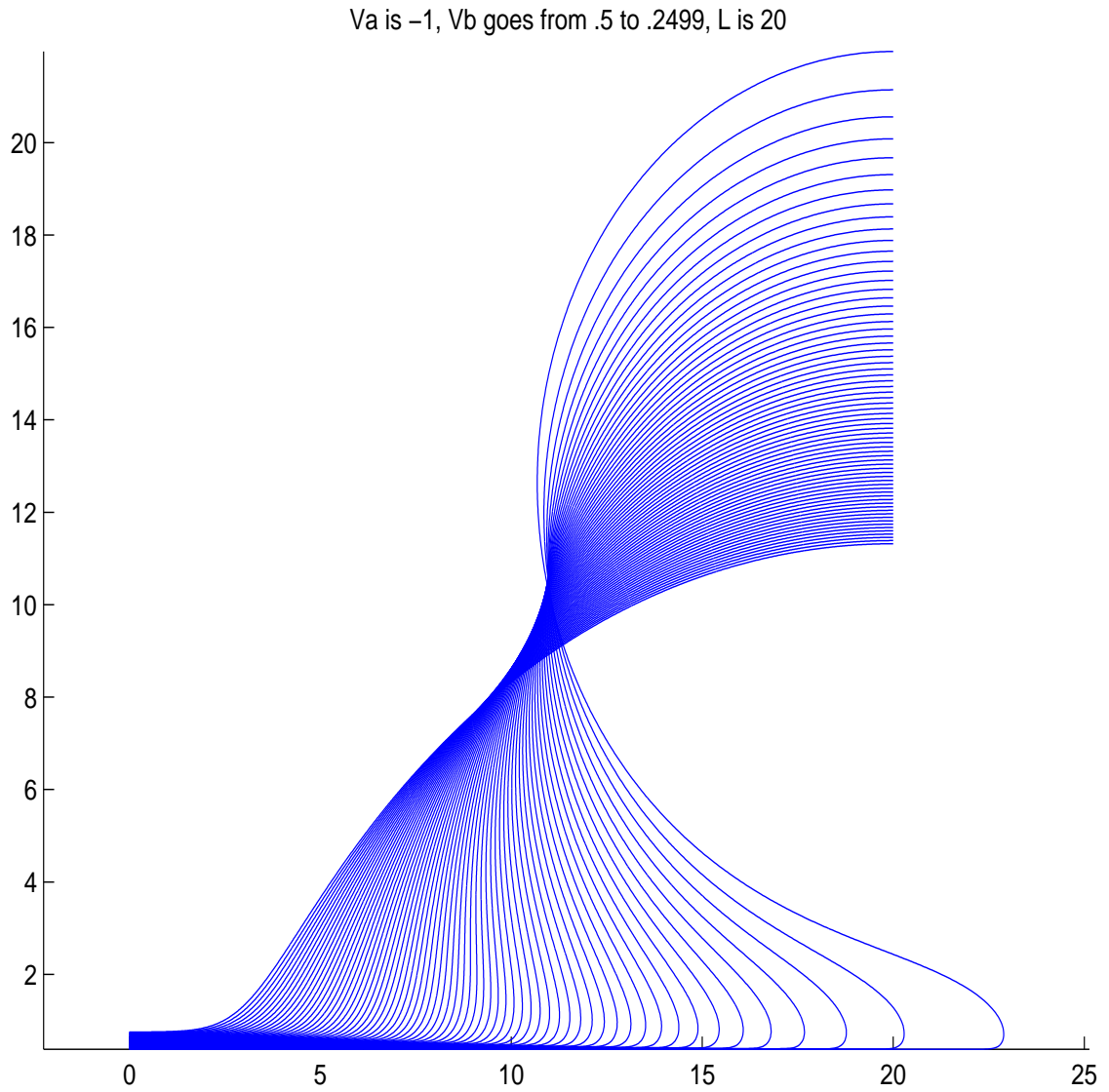
Figure 4.9: As the Van der Waals constant b is decreased, the depth of the precursor film decreases in proportion. Steeper droplets correspond to shallower precursor films. The droplet's foot eventually intersects the sidewall, pinching the droplet off from the precursor film.
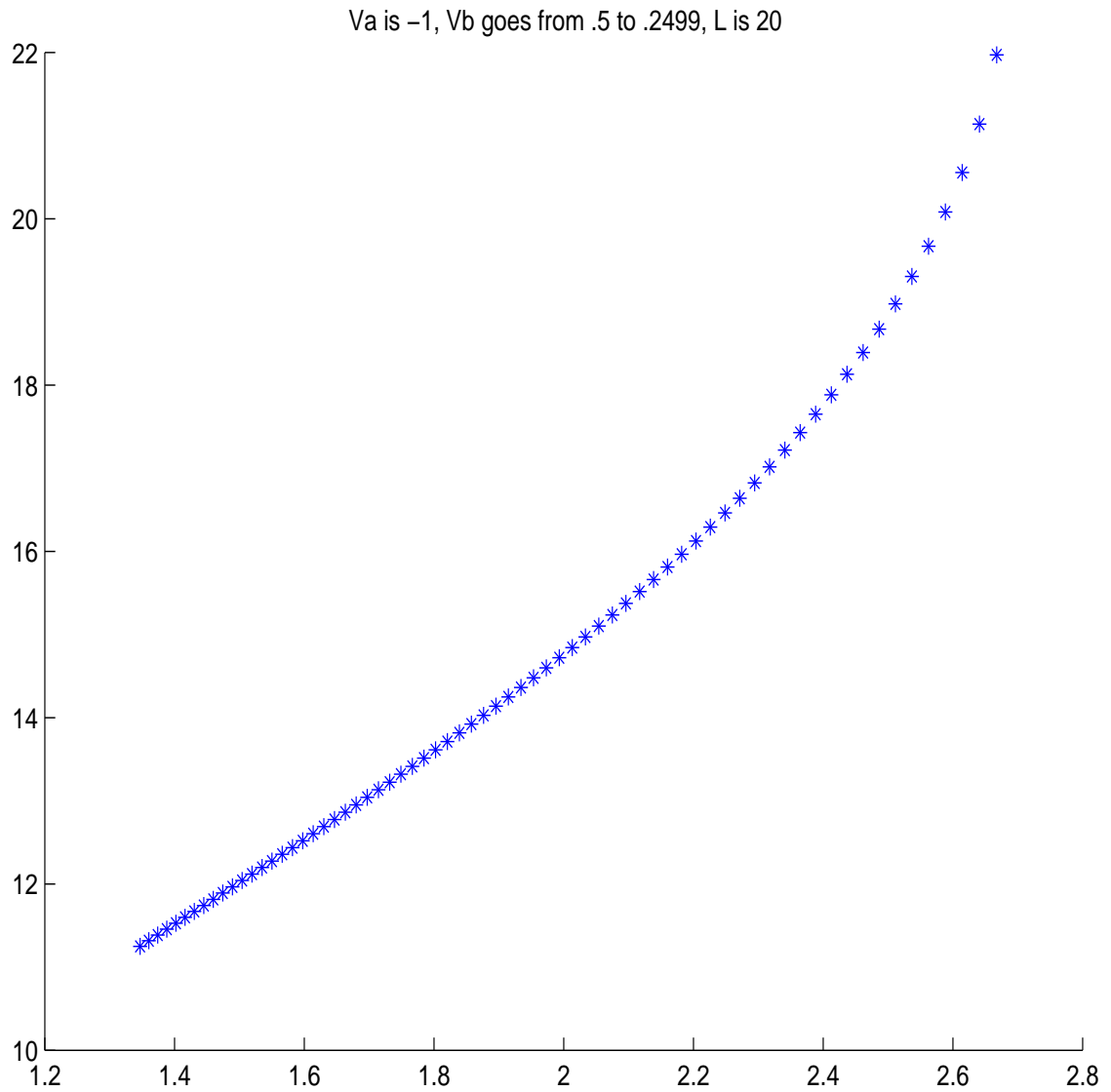
Figure 4.10: One over precursor depth, $\frac{1}{h_{min}} = \frac{2a}{3b}$, is plotted on the x-axis, and the droplet's height $h(L)$ at the box boundary is plotted on the y-axis. Our droplets' height increases without bound like those predicted by lubrication theory, but they pinch off and separate from the substrate at finite precursor height.

tionship. The model also predicts that decreasing precursor depth leads to droplet pinch-off rather than arbitrarily tall droplets, solving one of the major problems of the lubrication approximation.

4.4 Future work

I will be continuing work on this problem with Professor Bernoff this summer. The first thing we will do will be to allow point spacing to vary over the interface so that more points can be allocated at the droplet foot, where the interface is highly curved. This change should make it easier to follow the droplet branch as precursor depth and surface energy decrease, and it will certainly make it much easier to measure the contact angle accurately. Hopefully, we will be able to obtain more extensive and accurate data on the relationships between contact angle, droplet height, and the relative magnitudes of the energy terms.

When we have obtained satisfactory numerical data, we'll work on analysis. By the end of the summer, we would like to develop an understanding of the aforementioned relationships based on the analytical energy formulation. This will almost certainly require analytical modeling of the droplet foot by asymptotic matching.

After we understand this problem completely, we'll solve it for the axisymmetric geometry. This will require weighting the energy integral by the radius r.

$$
\begin{aligned}
E &= \int_0^R \Big[\sqrt{1 + h_r^2} - (\frac{a}{h^2} + \frac{b}{h^3})\Big] r \ dr \\
&= \int_0^{s(R)} \Big[\sqrt{r_s^2 + h_s^2} - (\frac{a}{h^2} + \frac{b}{h^3})\Big] r_s r \ ds
\end{aligned}
\tag{4.2}
$$

where s is the arc length along a radial cross-section. Changing the numerical code to use this energy formulation will be simple, but the analytical problem and the results will probably change significantly. In particular, the eigenfunctions of the

linear stability operator Ψ will become Bessel functions rather than cosines. The solutions to this problem will also carry more physical import than the planar-geometry solutions, since ridges of fluid tend to be unstable with respect to long-wave lateral perturbations and break up into axisymmetric droplets [14]. In addition, the axisymmetric model will allow us to capture the dynamics of the droplet pinch-off, which is perhaps our most important result.

Appendix A: Derivation of Van der Waals potentials

A.1 Dipole- induced dipole energy of interaction between a dipole and a polarizable molecule

The magnitude of an electric field a distance r away from a molecule with dipole moment $\vec{p}$ along the dipole axis is

$$\vec{E} = \frac{p}{2\pi\epsilon_0 r^3} \tag{A.1}$$

This dipole will induce a dipole moment in a neighboring molecule of polarizability α of

$$p_\alpha = \frac{-\alpha p}{2\pi\epsilon_0 r^3} \tag{A.2}$$

Approximating the induced dipole as two point charges q and $-q$ and linearizing the electric field over the small distance l between them, the magnitude of the attractive force between the dipole and the induced dipole is
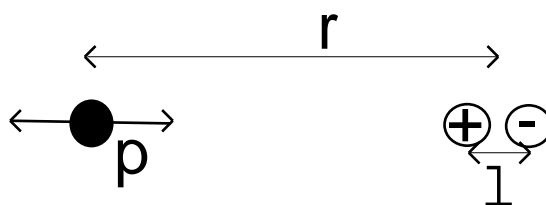

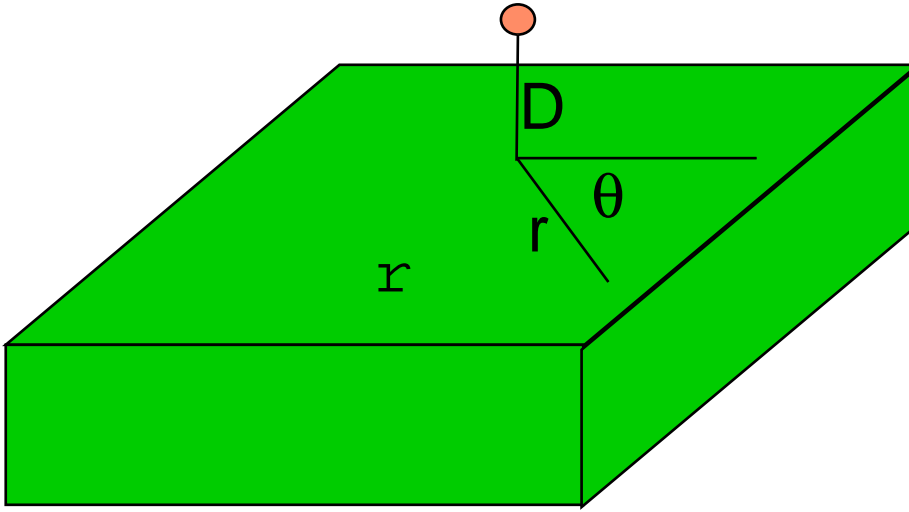Figure A.1: Interaction between a dipole and an induced dipole

Figure A.2: A dipole and a polarizable half- space

$$F \approx ql\frac{dE}{dr} \approx \alpha E\frac{dE}{dr} = \frac{-3p^2}{4\pi^2\epsilon_0^2 r^7} \tag{A.3}$$

and the energy of interaction is

$$w(r) = \int_{\infty}^{r} \frac{-3p^2 dr'}{4\pi^2\epsilon_0^2 r'^7} = \frac{-p^2}{8\pi^2\epsilon_0^2 r^6} \tag{A.4}$$

While this derivation is heuristic, it yields the correct scaling behavior for the dependence of $w(r)$ on r [13].

A.2 Energy of interaction between a dipole and a polarizable half-space

Absorbing all constants in equation (A.4) into a single constant C and working in cylindrical coordinates r, z, and θ, the net energy of interaction between and a polarizable half-space containing ρ molecules per unit volume separated by a distance D is [18]

$$w(D) = -C\rho \int_{\theta=0}^{2*\pi} \int_{z=0}^{\infty} \int_{r=0}^{\infty} \frac{rdrdx}{(z^2+r^2)^3} = \frac{2\pi C\rho}{4} \int_{z=D}^{\infty} \frac{dz}{z^4} = -\frac{2\pi C\rho}{12D^3} \tag{A.5}$$

A.3 Energy of interaction between a polarized fluid and a polarizable half-space

In equilibrium, the pressure P at the surface of a fluid film must be the same over the entire film:

$$P = f(h(x,y)) - \int_0^h \frac{dw(z(x,y))}{dz} dz \qquad (A.6)$$

where $f(h(x,y))$ includes pressure due to surface tension and any other sources and $w(z(x,y))$ is the dipole-half space potential found in the last section. This implies that the Van der Waals energy per unit area of a fluid of height $h(x,y)$ is equal to

$$-\int_0^h \int_0^h \frac{dw(z(x,y))}{dz} dz dz = -\int_0^h w(z(x,y)) dz \qquad (A.7)$$

Integrating the potential energy found in the last section from $z = 0$ will yield infinity. This problem can be circumvented by integrating from some small height δ which is guaranteed to be less than the height of the fluid; the energy of the fluid between $z = 0$ and $z = \delta$ is then common to all of the fluid and may be omitted from the energy. However, guaranteeing the existence of δ requires adding a repulsive term of the form $1/r^n$ where n is greater than 6 to the dipole-dipole potential Note that this term also provides a 'hard-core repulsion' between two dipoles and prevents the distance between them from going to zero.

Again absorbing all constants in Equation A.4 into a single constant C, the energy of interaction between a polarized fluid and a polarizable half space with ρ molecules per unit volume can be found by integrating the result found in the last section plus a repulsive term from δ to $h(x,y)$, the height of the fluid.

$$-\frac{2\pi C \rho_0 \rho_1}{12} \int_{x=-\infty}^{\infty} \int_{y=-\infty}^{\infty} \int_{z=\delta}^{h(x,y)} -\frac{1}{z^3} + \frac{1}{z^n} dz dx dy = \int_{x=-\infty}^{\infty} \int_{y=-\infty}^{\infty} W(h(x,y)) dx dy$$
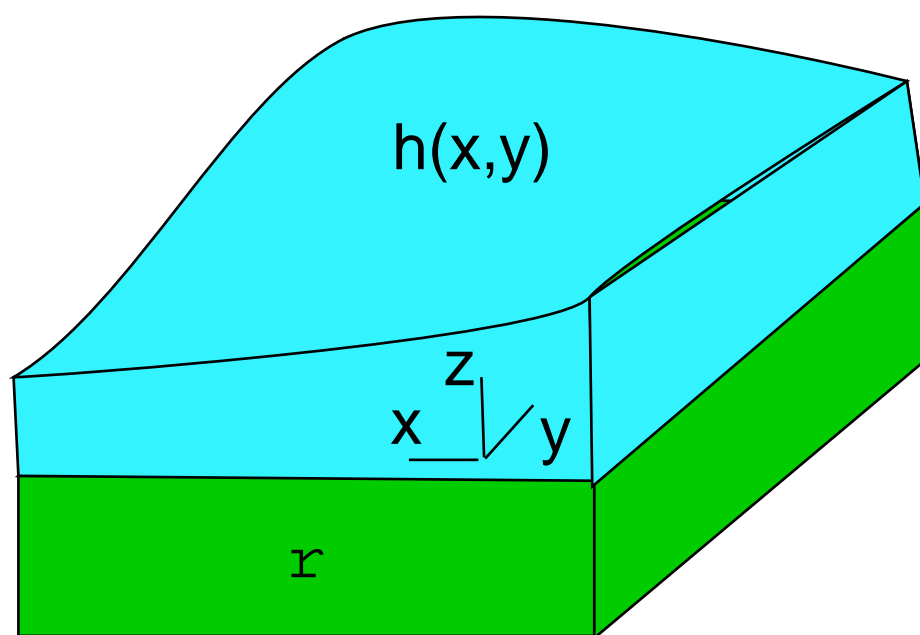
$$(A.8)$$

Figure A.3: A polarized fluid interacting with a polarizable half-space

This will be infinite, but the energy of interaction per unit surface area is finite. Neglecting the constant terms involving delta, $W(h(x,y))$ is equal to

$$\frac{1}{6}\pi C \rho \left(\frac{1}{2} \frac{n-1}{2(-1+n)(h(x,y))^2} - \frac{1}{(h(x,y))^{n-1}(-1+n)} \right) \qquad \text{(A.9)}$$

Bibliography

[1] J. Bischof *et al.* Dewetting modes of thin metallic films: Nucleation of holes and spinodal dewetting. *Phys. Rev. Lett*, 77:1536–1539, 1996.

[2] K. Stoev *et al.* The effects of thin films on the hydrodynamics near moving contact lines. *Physics of Fluids*, 10:1793–1803, 1998.

[3] L. Pismen *et al.* Spreading of a wetting film under the action of van der waals forces. *Phys. Fluids*, 12:480–483, 2000.

[4] M. Sferrazza *et al.* Interfacial instability driven by dispersive forces: The early stages of spinodal dewetting of a thin polymer film on a polymer substrate. *Phys. Rev. Lett.*, 81:5713–5716, 1998.

[5] Q. Chen *et al.* The velocity field near moving contact lines. *J. Fluid Mech.*, 337:49–66, 1997.

[6] R. Xie *et al.* Spinodal dewetting of thin polymer films. *Phys. Rev. Lett.*, 81:1251–1254, 1998.

[7] A. Bertozzi. Equilibria and stability in a regularized van der waals film. *Nonlinearity*, preprint:1–19, 2000.

[8] R. J. Burden and J. D. Faires. *Numerical Analysis*. Brooks/Cole, 7th edition, 2001.

[9] T. Erneux and S. Davis. Nonlinear rupture of free films. *Phys. Fluids*, 5:1117–1122, 1993.

[10] T. Erneux and D. Gallez. Can repulsive forces lead to stable patterns in thin liquid films? *Phys. Fluids*, 9:1194–1196, 1997.

[11] R. Konnur *et al.* Instability and morphology of thin liquid films on chemically heterogeneous substrates. *Phys. Rev. Lett.*, 94:931–934, 2000.

[12] S. Herminghaus *et. al.* Spinoidal dewetting in liquid crystal and liquid metal films. *Science*, 282:916–920, 1998.

[13] D. Griffiths. *Introduction to Electrodynamics*. Prentice Hall, 3rd edition, 1999.

[14] L. Hocking and M. J. Miksis. Stability of a ridge of fluid. *J. Fluid Mech.*, 246:157–177, 1993.

[15] L. M. Hocking. The influence of intermolecular forces on thin fluid layers. *Phys. Fluids*, 5:793–799, 1993.

[16] L. M. Hocking. The spreading of drops with intermolecular forces. *Phys. Fluids*, 6:3224–3228, 1994.

[17] L. M Hocking. The wetting of a plane surface by a fluid. *Phys. Fluids*, 7:1214–1220, 1995.

[18] J. Israelachvili. *Intermolecular and Surface Forces*. Academic Press, 2nd edition, 1992.

[19] J. B. Keller and G. J. Merchant. Flexural rigidity of a liquid surface. *J. Stat. Phys.*, 63:1039–1051, 1991.

[20] G. J. Merchant and J. B. Keller. Contact angles. *Phys. Fluids*, 4:477–485, 1992.

[21] V. S. Mitlin and N. V. Petviashvili. Nonlinear dynamics of dewetting: Kinetically stable structures. *Physica A*, 192:323–326, 1994.

[22] G. Reiter. The artistic side of intermolecular forces. *Science*, 282:888–889, 1998.

[23] A. Sharma and R. Khanna. Pattern formation in unstable thin liquid films. *Phys. Rev. Lett*, 81:3463–3465, 1998.

[24] E. B. Dussan V. and S. H. Davis. On the motion of a fluid-fluid surface along a solid interface. *J. Fluid Mech.*, 65:71–95, 1974.

[25] T. P. Witelski and A. J. Bernoff. Stability of self-similar solutions for van der waals driven thin film rupture. *Phys. Fluids*, 11:2443–2445, 1999.

[26] T. P. Witelski and A. J. Bernoff. Dynamics of three-dimensional thin film rupture. *Physica D*, preprint:1–29, 2000.